

A cross-correlation study of the Fermi-LAT γ -ray diffuse extragalactic signal

Jun-Qing Xia¹, Alessandro Cuoco², Enzo Branchini^{3,4,5}, Mattia Fornasa^{6,7}, Matteo Viel^{8,9}

¹ Scuola Internazionale di Studi Avanzati, Via Bonomea 265, I-34136, Trieste, Italy

² Stockholm University - Oskar Klein Center AlbaNova University Center, Fysikum, SE-10691, Stockholm, Sweden

³ Dipartimento di Fisica, Università degli Studi “Roma Tre”, via della Vasca Navale 84, I-00146 Roma, Italy

⁴ INAF, Osservatorio Astronomico di Brera, Milano, Italy

⁵ INFN, Sezione di Roma Tre, via della Vasca Navale 84, I-00146 Roma, Italy

⁶ Instituto de Astrofísica de Andalucía (CSIC), E18008, Granada, Spain

⁷ MultiDark fellow

⁸ INAF Osservatorio Astronomico di Trieste, Via G. B. Tiepolo 11, I-34141, Trieste, Italy

⁹ INFN, Sezione di Trieste, via Valerio 2, I-34127, Trieste, Italy

17 November 2021

ABSTRACT

In this work, starting from 21 months of data from the Fermi-Large Area Telescope (LAT), we derive maps of the residual isotropic γ -ray emission, a relevant fraction of which is expected to be contributed by the extragalactic diffuse γ -ray background (EGB). We search for the auto-correlation signals in the above γ -ray maps and for the cross-correlation signal with the angular distribution of different classes of objects that trace the large scale structure of the Universe. We compute the angular two-point auto-correlation function of the residual Fermi-LAT maps at energies $E > 1$ GeV, $E > 3$ GeV and $E > 30$ GeV well above the Galactic plane and find no significant correlation signal. This is, indeed, what is expected if the EGB were contributed by BL Lacertae (BLLacs), Flat Spectrum Radio Quasars (FSRQs) or star-forming galaxies, since, in this case, the predicted signal is very weak. Then, we search for the Integrated Sachs-Wolfe (ISW) signature by cross-correlating the Fermi-LAT maps with the WMAP7-Cosmic Microwave Background map. We find a cross-correlation consistent with zero, even though the expected signal is larger than that of the EGB auto-correlation. Finally, in an attempt to constrain the nature of the γ -ray background we cross-correlate the Fermi-LAT maps with the angular distributions of objects that may contribute to the EGB: QSOs in the SDSS -DR6 (Sloan Digital Sky Survey- Data Release 6) catalog, NRAO VLA Sky Survey (NVSS) galaxies, Two Micron All Sky Survey (2MASS) galaxies and Luminous Red Galaxies (LRGs) in the SDSS catalog. The cross-correlation is always consistent with zero, in agreement with theoretical expectations, but we find (with low statistical significance) some interesting features that may indicate that some specific classes of objects contribute to the EGB. A χ^2 analysis confirms that the correlation properties of the 21-month data do not provide strong constraints of the EGB origin. However, the results suggest that the situation will significantly improve with the 5- and 10-year Fermi-LAT data. The future EGB analysis will then allow placing significant constraints on the nature of the EGB and might provide in addition a detection of the ISW signal.

Key words: cosmology: theory – cosmology: observations – cosmology: large scale structure of the universe – gamma rays: diffuse backgrounds

1 INTRODUCTION

One of the most interesting open problems in astrophysics is the nature of the diffuse γ -ray background at GeV energies. The presence of a diffuse signal was first detected by the OSO-3 satellite (Kraushaar et al. 1972) with indications of both Galactic and isotropic diffuse emissions. SAS-2 (Fichtel et al. 1973) and

later EGRET (Sreekumar et al. 1998) revealed more clearly the isotropic component, which is commonly known as extragalactic γ -ray background (EGB). Although several local processes have been proposed to explain this background (Keshet et al. 2004; Moskalenko et al. 2006, 2007; Moskalenko & Porter 2009), the EGB is generally believed to be the superposition of contributions from unresolved extragalactic sources and, perhaps, diffuse GeV

emission processes like the annihilation of dark matter (DM) particles (Ullio et al. 2002). We will, however, in the following use the abbreviation “EGB”, even if the extragalactic origin of this component is still not fully clear.

Blazars are the most numerous population detected by EGRET and the Fermi Large Area Telescope (Fermi-LAT) (Hartman et al. 1999; Abdo et al. 2009). They have long been regarded as the most likely candidates to provide the bulk of the EGB emission. However, the recent analysis of the First Fermi-LAT AGN catalog obtained after ~ 1 year of data taking revealed that blazars can contribute $23 \pm 5\%$ (stat.) $\pm 12\%$ (syst.) of the EGB in the range between 0.1 and 100 GeV (Abdo et al. 2010d), disfavoring the interpretation of the EGB as mainly consisting of unresolved blazars. DM candidates in supersymmetric theories (as well as other WIMP candidates) can annihilate into GeV photons and contribute to the EGB (Ullio et al. 2002; Ando et al. 2007b; Pieri et al. 2009; Zavala et al. 2010, 2011). However, the amplitude and shape of the observed EGB spectrum (Abdo et al. 2010a,c) together with the available multi-wavelength and multi-messenger astrophysical constraints (Pato et al. 2009) seems to indicate that γ -ray photons from annihilation of WIMP-like Cold Dark Matter particles provide, at most, a minor contribution to the EGB. Finally, the EGB could be mainly consisting of a population of numerous but faint γ -ray sources: normal, star-forming galaxies are typical candidates that could make a substantial contribution to the EGB below 10 GeV (Pavlidou & Fields 2002; Fields et al. 2010).

To tackle the problem of the EGB nature one can use different and rather complementary methods (e.g. Hensley et al. (2009); Dodelson et al. (2009)) that may serve as independent constraints:

- Resolve the largest possible fraction of the EGB into individual sources. If the EGB were mainly contributed by a population of rare, bright objects, then Fermi-LAT will eventually be able to resolve a significant fraction of this radiation and to disentangle possible multiple components. If the EGB were mainly contributed by a population of common, faint objects, then only a few of them will be resolved by Fermi-LAT (see e.g. Pavlidou & Fields (2001) for the case of star-forming galaxies). Finally, if the EGB were significantly contributed by DM annihilations, then, the Fermi-LAT might be able to resolve only some individual sources associated to foreground dark Galactic subhalos, depending on the precise nature of the DM particle (Pieri et al. 2008, 2009).
- Compare the observed EGB energy spectrum with model predictions based on the luminosity function of some classes of objects and their energy spectra (e.g. Fields et al. (2010)).
- Analyze the one- or two-point statistics of the observed EGB photon counts to distinguish the contribution of clumpy components, typically associated to individual sources, to that of a diffuse component (Lee et al. 2009; Fields et al. 2010; Baxter et al. 2010; Slatyer & Finkbeiner 2010).
- Analyze the angular correlation properties of the EGB and compare it with those of a population of γ -ray emitting objects like blazars (Ando et al. 2007b,a), galaxy clusters (Miniati et al. 2007; Ando et al. 2007b) type Ia supernovae (Zhang & Beacom 2004) star-forming galaxies (Ando & Pavlidou 2009) and DM halos (Ando & Komatsu 2006; Ando et al. 2007b; Cuoco et al. 2007; Hooper & Serpico 2007; Cuoco et al. 2008; Siegal-Gaskins 2008; Taoso et al. 2009; Fornasa et al. 2009; Ando 2009; Cuoco et al. 2010).

In this work we follow the last approach and estimate the two-point angular auto-correlation function (ACF) of the Fermi-LAT EGB to identify those characteristic features that can be related

to the presence of a well defined population of objects. Due to its isotropy, the ACF signal of the EGB is expected to be weak. The signal can be amplified by cross-correlating the EGB with the angular distribution of the supposed EGB sources, since the number of contributing sources is typically large. For this reason we cross-correlate the EGB with different catalogs of extragalactic objects that can contribute to the EGB.

Our approach is very similar to that of Ando & Pavlidou (2009) but our analysis is more comprehensive in two aspects. First of all, since our aim is to identify the contributors to the EGB among a variety of possible candidates we cross-correlate the EGB maps with several different objects’ catalogs (SDSS-DR6 quasars (Richards et al. 2009), SDSS-DR6 Luminous Red Galaxies (Abdalla et al. 2008), NVSS radio galaxies (Blake & Wall 2002)) in addition to the 2MASS star-forming galaxies (Jarrett et al. 2000) considered by Ando & Pavlidou (2009). Second of all, not only we do provide theoretical predictions of the expected ACF and two-point cross-correlation function (CCF), but we actually estimate them from the 21-month Fermi-LAT data. Finally, we perform our analysis in configuration space (although we also show the angular power spectra for completeness) and consider energies $E > 1$ GeV, slightly higher than in Ando & Pavlidou (2009), to reduce the contamination of the signal due to the Galactic foreground.

In our work we also pursue another important goal: we attempt to detect the Integrated Sachs-Wolfe (ISW) signal (Sachs & Wolfe 1967). This effect is related to the variation over time of the gravitational potential Φ which arises at late cosmological times when dark energy or curvature become important, and induces additional anisotropies in the Cosmic Microwave Background (CMB) at large angular scales. The effect is instead absent during the matter dominated era when the gravitational potential is constant, and, for this reason, is a potentially powerful probe for dark energy. Successful searches for the ISW effect have been performed in the past by cross-correlating the CMB maps with the large scale structures probes that we have already mentioned (NVSS radio galaxies (Nolta et al. 2004; Raccanelli et al. 2008; Xia et al. 2010), 2MASS galaxies (Afshordi et al. 2004; Rassat et al. 2007), SDSS quasars (Giannantonio et al. 2006; Xia et al. 2009)), SDSS galaxies (Cabr e et al. 2006, 2007) and with combinations of different tracers (Giannantonio et al. 2008; Ho et al. 2008; Hirata et al. 2008). Besides the above surveys, also the EGB sources are a probe of the large scale structures, and cover a large fraction of the sky. Thus, we do expect some ISW signal which could be detected through the cross-correlation between Fermi and CMB data. Therefore, in this paper we use the cross-correlation between the 21-month Fermi-LAT EGB maps with the WMAP7 maps (Komatsu et al. 2010) of the CMB to look for the ISW signal.

Our analysis is also similar to that of Boughn et al. (1998) and Boughn & Crittenden (2004) since, like in their case, we also cross-correlate two diffuse signals. In our case it is CMB versus EGB whereas in their case the CMB is cross-correlated with hard X-ray background. However, for us, due to the large errors caused by a smaller number of photons, we do not expect to be able to put useful constraints on the cosmological constant or on the bias of γ -ray sources. Instead, we will use the cross-correlation analysis to constrain the nature of the EGB in the framework of the concordance Cold Dark Matter model with a cosmological constant (Λ CDM). Here we adopt the best-fit WMAP model (Komatsu et al. 2010) in which $\Omega_b h^2 = 0.02267$, $\Omega_c h^2 = 0.1131$, $\tau = 0.084$, $h = 0.705$, $A_s = 2.15 \times 10^{-9}$ at $k_0 = 0.05 \text{ Mpc}^{-1}$, and $n_s = 0.968$.

The layout of the paper is as follows: in Section 2 we briefly review the theoretical description of the cross-correlation analysis,

including the ISW signal. In Section 3 we present the various maps used to compute the two-point ACF and CCF. We describe the statistical estimator used to evaluate the auto- and cross-correlation functions in Section 4. The results of the cross-correlation analysis are presented in Section 5, analyzed in Section 6 and discussed in Section 7. The conclusions are presented in Section 8.

2 THEORY

Our theoretical formulation of the mean γ -ray emission contributed by unresolved sources, their auto-correlation and cross-correlation with the angular distribution of different types of extragalactic objects follows that of Ando & Pavlidou (2009). The treatment of the cross-correlation with the CMB maps and the related ISW theory follows that of Boughan et al. (1998) and Xia et al. (2009).

2.1 Mean Intensity

The mean differential γ -ray *energy flux* due to a population of sources j characterized by a γ -ray luminosity function $\Phi_j(L_\gamma, z)$ is:

$$\frac{dI_j}{dE} = \frac{c}{4\pi} \int \left[\int_{L_{\text{MIN}}}^{L_{\text{MAX}}(z)} \Phi_j(L_\gamma, (1+z)E, z) L_\gamma dL_\gamma \right] \frac{dz}{(1+z)H(z)}, \quad (1)$$

where E is the energy, z is the redshift, $H(z) = H_0[(1+z)^3 \Omega_M + \Omega_\Lambda]$ is the expansion history of a flat universe with a cosmological constant Λ and the $(1+z)^{-1}$ term represents cosmological dimming of the photon energy. L_γ is the source luminosity, given throughout the paper in erg s^{-1} , while we measure dI_j/dE in $\text{erg cm}^{-2} \text{s}^{-1} \text{sr}^{-1}$. $\rho_\gamma(z) \equiv \int \Phi(L) L dL$ represents the comoving γ -ray luminosity density of the sources at redshift z . The integration limits are set by requiring that the EGB consists entirely of sources below the *photon* flux detection limit S_{lim} ($\text{ph cm}^{-2} \text{s}^{-1}$). In this case $L_{\text{MAX}}(z) = 4\pi d_L^2(z) F_{\text{lim}} (1+z)^{-2+\Gamma_j}$ (Ghisellini et al. 2009), where d_L is the luminosity distance in the adopted cosmology and Γ_j is the *photon* index of the source population energy spectrum, assumed to be a power law (see also below). F_{lim} is the *energy* flux detection limit ($\text{erg cm}^{-2} \text{s}^{-1}$), which is related to the photon flux S_{lim} through $F_{\text{lim}} = S_{\text{lim}} E_i \times (1-\Gamma_j)/(2-\Gamma_j)$, where E_i is the energy threshold of integration, typically 100 MeV. L_{MIN} can be, in principle, set to zero if the total luminosity density $\rho_\gamma(z)$ were convergent. Unluckily, for the source classes discussed below the extrapolation of the luminosity function to small values of L_{MIN} gives a divergent total luminosity. However, an effective L_{MIN} , if not given *a priori*, can be nonetheless computed by extrapolating the observed $\Phi_j(L)$ and by requiring that the population of sources j contribute a fraction f_j of the total EGB:

$$f_j \int_{100}^{+\infty} \frac{dI_{\text{EGB}}}{dE} \frac{dE}{E} \equiv \int_{100}^{+\infty} \frac{dI_j}{dE} \frac{dE}{E} = \int_0^{S_{\text{lim}}} \frac{dN_j}{dS_{100}} S_{100} dS_{100}, \quad (2)$$

where dN_j/dS_{100} represents the differential counts of j sources and the factor of E^{-1} accounts for the units of the dN_j/dS_{100} function typically given in terms of photon flux rather than energy flux (Abdo et al. 2010d). The conventional threshold of 100 MeV has been chosen to define the integral flux above 100 MeV S_{100} . This expression assumes that the detection efficiency can be modeled as a step function. In fact Abdo et al. (2010d) found that the Fermi-LAT detection efficiency for $E > 100$ MeV drops as S^{-2} below $S_{\text{lim}} = 3 \times 10^{-8} \text{ ph cm}^{-2} \text{s}^{-1}$. We verified that, varying S_{lim} in the reasonable interval 10^{-8} - $10^{-7} \text{ ph cm}^{-2} \text{s}^{-1}$, this stepwise

approximation does not affect significantly the resulting redshift distribution of unresolved sources. From Eqs. 1 and 2 then it is possible to compute the mean differential flux and the fraction f_j of the EGB emission contributed by any class of unresolved sources once their luminosity function and number counts are modeled theoretically or extrapolated from observations.

In this work we will assume that unresolved sources have power law energy spectra $I(E)dE \propto E^{1-\Gamma_j} dE$ and photon index $\Gamma_j > 1$. In this case the energy dependence drops out of the integral in Eq. 1 and the integrated energy flux becomes:

$$I_j(> E) = \int_E^\infty \frac{dI_j}{dE} dE = \frac{cE^{2-\Gamma_j}}{4\pi} \int \left[\int_{L_{\text{MIN}}}^{L_{\text{MAX}}(z)} \Phi_j(L_\gamma, z) L_\gamma dL_\gamma \right] \frac{(1+z)^{-\Gamma_j}}{H(z)} dz. \quad (3)$$

In this paper we deal with maps of photon counts rather than energy flux; the photon flux (above energy E) being simply $(2-\Gamma_j)/(1-\Gamma_j) \times I_j(> E)/E$. We will consider integrated fluxes with three energy thresholds: $I(> E = 1\text{GeV})$, $I(> E = 3\text{GeV})$ and $I(> E = 30\text{GeV})$ and three possible contributors to the EGB: two types of blazars, Flat Spectrum Radio Quasars (FSRQs) and BL Lacertae (BLLacs), and star-forming galaxies. The main characteristics of these three populations, summarized in Table 1, are:

(i) *FSRQs* represent a sub-class of blazars, i.e. AGNs with a relativistic jet pointing close to the line of sight. For the classification of blazars as FSRQs we rely on the criteria adopted by Abdo et al. (2009). These authors also compute the FSRQs luminosity function for $E > 100$ MeV in three different redshift intervals, and we adopt their description under the assumption that its shape does not depend on the energy band. The FSRQs number counts have been measured by Abdo et al. (2010d) from a larger sample of objects. The slope of the counts flattens in the faint end, implying that FSRQs at most contribute to $f_j \sim 25\%$ of the EGB. Their spectra are steeper than those of BLLacs, with an average photon index of $\Gamma \sim 2.47$. To model the FSRQs contribution to EGB we have derived an f_j estimate from the $\log N$ - $\log S$ of Abdo et al. (2010d). We then use the luminosity function and, as anticipated, we enforce an *effective* luminosity cut L_{MIN} . The calculation gives $L_{\text{MIN}} = 0.2 \times 10^{48} \text{ erg s}^{-1}$. The resulting redshift distribution of the flux is shown in Fig. 1, with the apparent piecewise behavior resulting from the different luminosity functions in the different redshift bins. We stress that the value of L_{MIN} derived in this way is not fully consistent with the minimum FSRQ luminosity measured by Abdo et al. (2009). This affects the redshift distribution in the lowest redshift bin, which however makes only a subdominant contribution to the total flux. Given the large uncertainties in the modeling of the FSRQs luminosity functions and their counts, this is likely a reasonable level of approximation. Finally, for these sources we adopt the redshift-dependent AGN biasing function proposed by Bonoli et al. (2009) in the framework of the semi-analytic models of AGN-black holes co-evolution: $b_\gamma(z) = 0.42 + 0.04(1+z) + 0.25(1+z)^2$.

(ii) *BLLacs* are another sub-class of blazars, on average less-bright than FSRQs. As in the previous case we adopt the BLLacs luminosity function measured by Abdo et al. (2009), the number counts determined by Abdo et al. (2010d) and enforce an effective value of L_{MIN} to reconcile the two predictions. The corresponding contribution to the EGB is $f_j \sim 12\%$, while $L_{\text{MIN}} = 6 \times 10^{43} \text{ erg s}^{-1}$. Finally, we use the average photon index measured by Abdo et al. (2010d), i.e. $\Gamma \sim 2.2$ and assume that BLLacs

and FSRQs have the same bias factor $b(z)$. In this case the luminosity function is compatible with no-evolution in the different redshift bins and the corresponding redshift distribution in Fig. 1 has no piecewise behavior.

(iii) *Star-forming galaxies* are fainter and much more common than blazars. In fact, it has been proposed that they alone could account for the EGB fraction which is not contributed by unresolved blazars. Fields et al. (2010) have shown that under the assumption of an Euclidean faint-end slope for the source counts, their contribution to the EGB can be as large as $f_j = 70\%$, an assumption that we will also adopt in our analysis. Since they are very faint and difficult to resolve, their luminosity function cannot be determined experimentally but needs to be modeled theoretically. Ando & Pavlidou (2009) have proposed a model in which the luminosity of each single source scales with the star-formation rate and the gas mass fraction. Since in this model the γ -ray emissivity is rescaled from that of the Milky Way, the underlying assumption is that most of the γ -ray photons are emitted from de-evolved versions of our own Galaxy. Current theoretical uncertainties and weak observational constraints do not allow to discriminate among the simple model proposed by Ando & Pavlidou (2009) and the more recent (and more sophisticated) one presented by Fields et al. (2010). For this reason in this paper we have decided to adopt the first one. The energy spectrum of star-forming galaxies is characterized by a strong pionic peak at $E \sim 0.2$ GeV, a feature that also determines the energy dependence of their contribution to the EGB. In the energy range we are interested in ($E > 1$ GeV), their energy spectrum is fairly well approximated by a power law behavior with $\Gamma \sim 2.475$ (Fields et al. 2010) that allows us to use Eq. 3. Finally, we assume that star-forming galaxies are unbiased, i.e. $b_S = 1$, as suggested by observations (Afshordi et al. 2004). The results of the auto- and cross-correlation studies do not change significantly as long as the bias of these galaxies is close to unity (Ando & Pavlidou 2009).

In Fig. 1 we show the redshift dependence of the normalized energy flux per unit redshift $d \ln I(> E)/dz$ for the three proposed EGB sources: FSRQs (red, dashed), BLLacs (black, continuous) and star-forming galaxies (blue, dot-dashed). This function, proportional to the integrand in Eq. 3, represents the contribution to the EGB from the sources in a specific redshift range. In the BLLacs scenario, the contribution to the EGB signal is relatively local, i.e. produced by a population of faint, nearby sources. In the FSRQs case the signal mostly comes from $z \geq 2$ and drops to zero at $z < 0.9$. This reflects the fact that FSRQs are rare bright objects which, for $z < 0.9$, would have $L_{max} < L_{MIN}$ in Eq.1, i.e. would be above detection threshold and removed from the map. As a consequence, the cross correlation of the FSRQs signal with catalogs of objects whose number density peaks at low redshifts is expected to be zero, as we shall see in Section 5. Star-forming galaxies represent an intermediate case in which the signal is produced over a relatively broad redshift range around $z \sim 1$.

2.2 Fluctuations in the γ -ray flux

To compute the predicted auto- and cross-correlation signals we need to model the fluctuations of the γ -ray flux. These fluctuations arise from local deviations from the γ -ray luminosity density $\rho_\gamma(z)$ that we assume to be proportional to the deviations from the mean number density of sources $n_\gamma(z) \equiv \int \Phi(L) dL$:

$$\delta_\gamma(z, \mathbf{x}) \equiv \frac{\rho_\gamma(z, \mathbf{x}) - \rho_\gamma(z)}{\rho_\gamma(z)} = \frac{n_\gamma(z, \mathbf{x}) - n_\gamma(z)}{n_\gamma(z)} \equiv \delta_{n_\gamma}(z, \mathbf{x}). \quad (4)$$

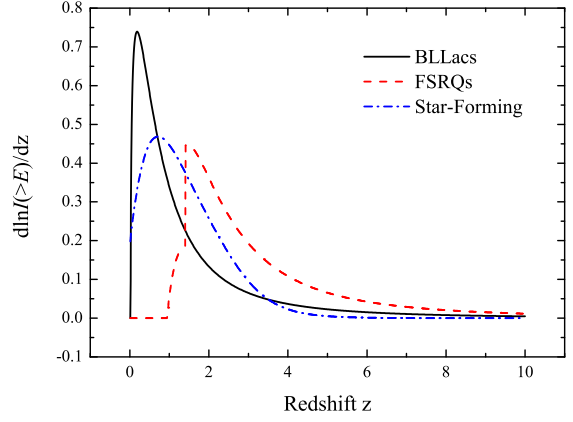


Figure 1. Normalized γ -ray flux per unit redshift $d \ln I(> E)/dz$ as a function of z for three different source classes: FSRQs (red, dashed), BLLacs (black, continuous) and star-forming galaxies (blue, dot-dashed).

Table 1. Investigated EGB contributors. All values refer to $E > 3$ GeV and $S < S_{lim}$. The luminosity function, $\frac{dN}{dS}$ and spectral parameters for FSRQs and BLLacs are taken from Abdo et al. (2009) and Abdo et al. (2010d).

Source Type	f_j	$\Phi(L_\gamma, z) \propto L^{-\alpha}$	$\frac{dN}{dS} \propto S^{-\beta}$	$I(E) \propto E^{-\Gamma}$
FSRQs	25 %	$\alpha = 1.57 \quad z < 0.9$	$\beta = 1.72$	$\Gamma = 2.47$
		$\alpha = 2.45 \quad z = [0.9, 1.4]$		
		$\alpha = 2.58 \quad z > 1.4$		
BLLacs	12 %	$\alpha = 2.23 \quad z \geq 0$	$\beta = 0.70$	$\Gamma = 2.20$
Star-form.	70 %	See Text	$\beta = 2.5$	$\Gamma = 2.45$

We also assume that the γ -ray sources trace the underlying fluctuations in the mass density according to some linear biasing prescription that may depend on the redshift:

$$\delta_{n_\gamma}(z, \mathbf{x}) \equiv b_\gamma(z) \delta_m(z, \mathbf{x}) = b_\gamma(z) \frac{\rho_m(z, \mathbf{x}) - \rho_m(z)}{\rho_m(z)}, \quad (5)$$

where ρ_m indicates the mass density and $b_\gamma(z)$ is called the biasing function.

Putting all together, the expected fluctuation in γ -ray energy flux is:

$$\delta I(\mathbf{n}) \equiv \frac{I(\mathbf{n}) - I}{I} = \frac{\int (1+z)^{-\Gamma} H(z)^{-1} \rho_\gamma(z) b_\gamma(z) \delta_m(z, \mathbf{x}) dz}{\int (1+z)^{-\Gamma} H(z)^{-1} \rho_\gamma(z) dz}, \quad (6)$$

where $I \equiv I(> E)$ indicates the γ -ray mean flux and $I(\mathbf{n}) \equiv I(> E, \mathbf{n})$ is the energy flux along the generic direction \mathbf{n} .

2.3 Two-point Angular Correlation Function and Spectrum

We can now compute the expressions for the two-point ACF of the EGB fluctuation field E and the two-point CCF between E and another fluctuation field obtained from a source catalog, S .

The general expression for the two-point angular correlation is

$$\langle \delta I(\mathbf{n}_1) \delta J(\mathbf{n}_2) \rangle = \sum_l \frac{2l+1}{4\pi} C_l^{JJ} P_l[\cos(\theta)], \quad (7)$$

where I and J are the two fields and the angular spectrum is given by:

$$C_I^J = \frac{2}{\pi} \int k^2 P(k) [G_I^I(k)] [G_J^J(k)] dk. \quad (8)$$

and $P(k)$ is the present-day power spectrum.

For example, for the EGB ACF one has $I = J = E$ with

$$G_I^E(k) = \frac{\int (1+z)^{-\Gamma} H(z)^{-1} \rho_\gamma(z) b_\gamma(z) D(z) j_l[k\chi(z)] dz}{\int (1+z)^{-\Gamma} H(z)^{-1} \rho_\gamma(z) dz}, \quad (9)$$

where $j_l[k\chi(z)]$ are spherical Bessel functions, $D(z)$ is the linear growth factor of density fluctuations and $\chi(z)$ is the comoving distance to redshift z . In our analysis, we use the public code CAMB (Lewis & Bridle 2002) to generate the linear power spectrum of density fluctuations and the HALOFIT (Smith et al. 2003) built-in routine for non-linear correction to obtain the fully-evolved, non-linear matter power spectrum $P(k)$ at any epoch. We note that non-linear corrections do not affect our results significantly.

In case of cross-correlation with a fluctuation field of discrete, unresolved sources one has $I = E$, $J = S$ and

$$G_I^S(k) = \int \frac{dN(z)}{dz} b_S(z) D(z) j_l[k\chi(z)] dz, \quad (10)$$

where $dN(z)/dz$ and $b_\gamma(z)$ represents the redshift distribution and the bias factor of the sources that do not necessarily coincide with the γ -ray sources.

Finally, if one cross correlates EGB with another diffuse signal, like the temperature fluctuation field obtained from the CMB maps ($I = E$, $J = T$) then

$$G_I^T(k) = -2 \int \frac{d\Phi(k)}{dz} j_l[k(z)] dz, \quad (11)$$

where Φ represents the gravitational potential.

In this case the cross-correlation signal in Eq. 7 represents the ISW effect, expected if the EGB were contributed by sources that trace the underlying mass distribution.

In Section 5 we will use Eqs. 7, 8, 9, 10 and 11 to predict the expected auto- and cross-correlation signal that will be compared with data.

3 MAPS

In this section we describe the various maps (residual isotropic Fermi-LAT maps, WMAP7 CMB, SDSS QSOs, SDSS, LRGs, 2MASS galaxies, NVSS radio galaxies) that will be used for the auto- and cross-correlation analysis.

3.1 Fermi-LAT maps

The Large Area Telescope (LAT) is the primary instrument onboard the Fermi Gamma-ray Space Telescope launched in June 2008 (Atwood et al. 2009). It is a pair-conversion telescope covering the energy range between 20 MeV and 300 GeV. Due to its excellent angular resolution ($\sim 0.1^\circ$ above 10 GeV), very large field of view (~ 2.4 sr) and efficient rejection of background from charged particles, it represents a key experiment for γ -ray astronomy. Fermi-LAT is continuously scanning the sky in survey mode, providing a complete image of the sky every 3 hours.

The data gathered by the telescope are available online ¹. For

the present analysis we used, unless otherwise specified, 21 months of data. We used only events classified as *class 4*. *Class 4* events form the dataset with the lowest level of CR background contamination currently available for LAT data analysis. Details on this event classification are described in Abdo et al. (2010c). We also use events labeled as *class 3* (cf. Atwood et al. (2009)) for consistency checks ². *Class 3* events have a larger residual contamination. We apply a cut of 100° on the zenith angle, 52° on the satellite rocking angle and 65° on the inclination angle to reduce the contamination from Earth albedo. The counts then have been pixelized in the HEALPix format (Górski et al. 2005) with $N_{\text{side}} = 64$, corresponding to $N_{\text{pix}} = 49152$ pixels with an angular size $0.92^\circ \times 0.92^\circ$. The majority of these events come from the resolved point sources (Abdo et al. 2010b) and from the Galactic diffuse emission due to γ -rays produced in the interaction of cosmic rays with the interstellar medium. Both need to be removed to extract the EGB signal.

To account for the Galactic diffuse foreground we adopted the model `gll_iem_v02.fit` ³. In the following this will be referred to as *V1*. The model is based on fits of the LAT data to templates of the HI and CO gas distribution in the Galaxy as well as an Inverse Compton model obtained with the GALPROP code ⁴ and a further template for the Loop-I region (Casandjian et al. 2009). The model, based on 1 year of data taking by Fermi-LAT, describes well the Galactic diffuse emission over the sky, with some exception, most prominently in the regions which have been associated with giant gamma-ray lobes (Su et al. 2010). We will thus also use a preliminary version of a refined model in development, which, further, includes templates specifically for these structures, sensibly reducing the residuals in these regions. This is model *V2*. In the next section we check the impact of these models on the ACFs-CCFs and compare the results with those obtained by masking out the areas where the Bubble and Loop-I emission are more prominent. The mask is obtained from the tabulated contours given in (Su et al. 2010) excluding the whole region enclosed by Loop-I in the North Galactic sky. In addition, for both models, we masked out a 20° strip above and below the Galactic plane where the EGB signal is largely subdominant. And in order to check the robustness of our results, we vary the strip mask width from $b = 20^\circ$ to $b = 50^\circ$, in steps of $\Delta b = 10^\circ$.

Point sources in the 1 year Fermi-LAT point-source catalogue 1FGL (Abdo et al. 2010b) are also masked as described in Cuoco et al. (2010). The point source masking is adaptive, in the sense that more intense sources, more likely to bias the results, are masked with a larger circle (up to 2-3 degree radius), while fainter ones are masked with a smaller circle down to about 1 degree (see Fig. 2).

To subtract the Galactic foreground from the data we have first generated the energy dependent exposure maps with the `gtxpcube` routine available in the public Fermi-LAT science tools ⁵. Version `p6v3 class 4` of the LAT instrument response functions (IRFs) and the same cuts used for the event selections were used for the exposure map generation. Maps of expected foreground counts from our two adopted Galactic diffuse emission

² *Class 4* events are also referred to as “*dataclean*” class while the union of *class 3* and *class 4* events is also referred to as “*diffuse*” class. See http://fermi.gsfc.nasa.gov/ssc/data/analysis/documentation/Cicerone/Cicerone_Data_Exploration/Data_preparation.html

³ A more detailed description can be found at <http://fermi.gsfc.nasa.gov/ssc/data/access/lat/BackgroundModels.html>

⁴ <http://galprop.stanford.edu/>

⁵ See <http://fermi.gsfc.nasa.gov/ssc/>

¹ <http://fermi.gsfc.nasa.gov/ssc/data/access/>

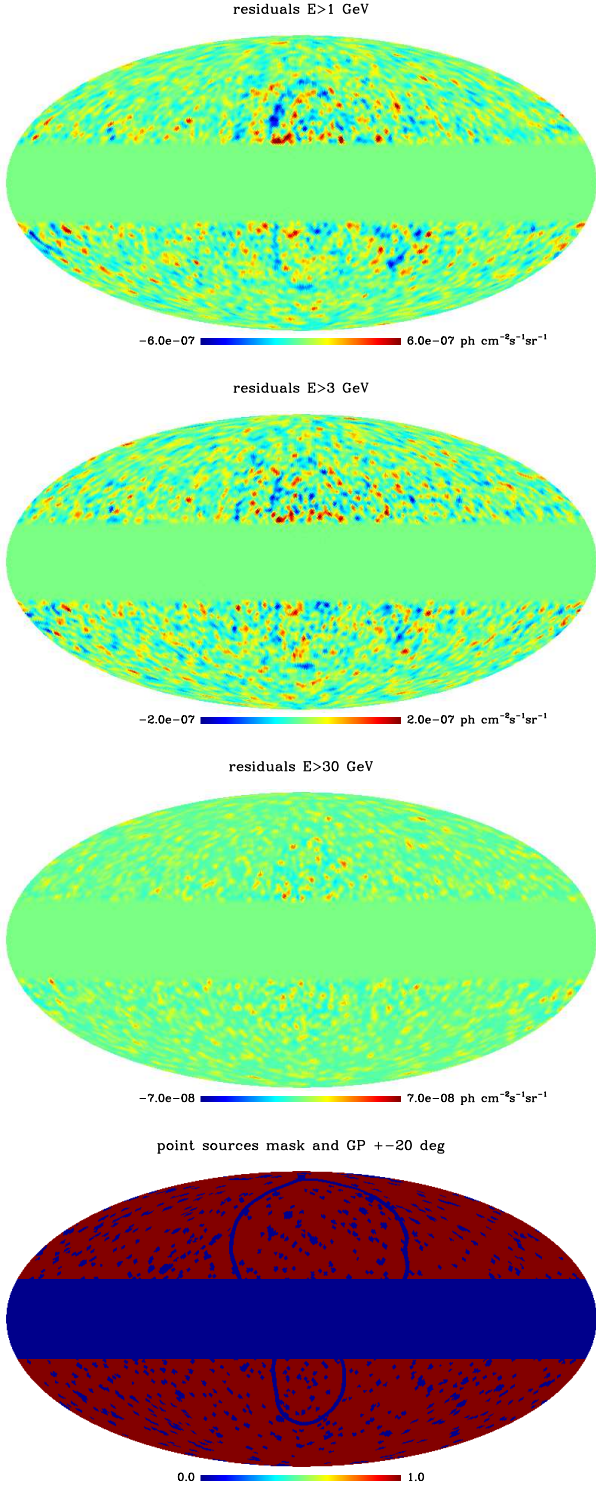


Figure 2. Residual gamma-ray emission obtained from analyzing 21 months of Fermi-LAT data for energies $E > 1$ GeV (top), $E > 3$ GeV (second from the top), $E > 30$ GeV (second from the bottom) and the mask covering the point sources in the 1 year Fermi-LAT point sources catalog and the region with $|b| < 20^\circ$ (bottom panel). The two contours in the mask indicate the regions which are further removed when the Lobes/Loop-I mask is applied. The residual maps have been smoothed with a 2° Gaussian filter to remove small scale Poisson noise. All maps are in Galactic coordinates and have a resolution $N_{\text{side}} = 64$ ($\sim 0.92^\circ$). All Fermi-LAT maps have been cleaned by removing the V2 Galactic model and all multipoles with $\ell \leq 10$ (see text).

models have been calculated by applying the exposure maps to the models and convolving them with the Point Spread Function (PSF) of the LAT averaged over the field of view and the relevant energy range. The `GaRDian` package (Ackermann et al. 2008) was used for this task. We thus include explicitly the PSF convolution, although we stress that in the energy range considered the PSF width is always smaller or at most comparable to our minimum angular bin (approximately 1°). However, further checks of the effect of the PSF on the ACF are considered in the next section. After the subtraction, the residuals should be dominated by the EGB signal and by the residual isotropic instrumental background. We have produced three maps containing events with energy $E > 1$ GeV, $E > 3$ GeV and $E > 30$ GeV, respectively. The energy cut was performed to reduce the chance of residual contamination from Galactic emission and to evaluate different trade-offs between clean maps and reasonably large statistics.

Since models V1 and V2 are not perfect, residuals can contain some spurious signal on large scales that may affect the correlation studies. The impact on the CCF is small since these spurious residuals are not expected to correlate with the extragalactic signal, but might be significant on the ACF. For all the maps, we thus always remove the residual monopole and dipole contribution. This is performed using the specific HEALPix routine, `remove_dipole`. In addition, we have implemented a more aggressive cleaning procedure in which, besides removing the monopole and dipole, we have expanded the residual maps into spherical harmonics using the HEALPix tool `anafast` and have removed all the multipoles up to $\ell = 10$ that contribute to the large scale signal. We will refer to the residual maps with all $\ell < 10$ multipoles removed as $\ell 10$ maps whereas $\ell 1$ indicates the maps in which only dipole and monopole have been removed. The validation of this procedure and testing for possible, undesired systematic effects is described in the next section.

The three $\ell 10$ residual counts maps are shown in Fig. 2 together with our fiducial mask removing the region within 20 degrees from the Galactic Plane and the point sources. To better illustrate the fluctuation properties of these maps, the mean has been removed, thus showing only fluctuations around zero. Furthermore, the maps have been smoothed with a 2° Gaussian filter to remove small scale Poisson noise.

3.2 Validation and checks

The scope of this section is to describe the various tests that we have performed to check and validate our cleaning procedure, to reveal the presence of possible systematic effects, to correct them and estimate their impact on the ACF and CCF analysis. For brevity we only show a subset of the results obtained, but we stress that all robustness tests described in this section have been repeated for each of the ACF/CCFs analyses presented in this paper.

3.2.1 Validating the $\ell 10$ cleaning procedure

To validate the $\ell 10$ cleaning procedure we have applied this cleaning technique to a set of mock data mimicking the characteristics of the real 21-month Fermi-LAT data. The mock, Monte Carlo-generated data-sets are simulated with the `gtobssim` routine using the `p6_v3_diffuse` Instrument Response Functions and including the contribution from three signals (i) a Galactic diffuse component generated using the V1 Galactic model, (ii) an extragalactic diffuse and isotropic component (hence with no intrinsic

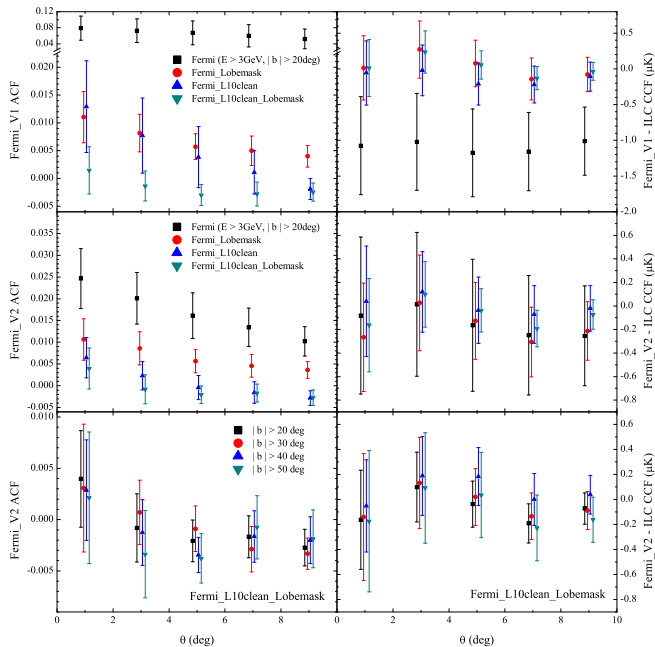


Figure 3. ACFs (left panels) and CCFs with the CMB (right panels) for different cleaning procedures ($\ell 10$ and $\ell 1$, with/without Bubbles/Loop-I mask) for the $V1$ Galactic model (top panels), $V2$ Galactic model (middle panels), and for different Galactic latitude cuts (bottom panels). All plots refer to Fermi $E > 3$ GeV residual maps.

ACF) generated with the `isotropic_iem_v02.txt`⁶ model and (iii) a signal contributed by a population of AGNs generated by sampling their observed $\log N$ - $\log S$ distribution (Abdo et al. 2010d) of which we mask the 1200 brightest ones. No intrinsic clustering is assumed for the simulated AGNs which are distributed across the sky randomly. The same pipeline described in the previous section is then applied to the mock datasets to obtain the residual maps from which ACFs and CCFs with the CMB are calculated. We observe that the resulting ACFs and CCFs are generally nicely consistent with zero. Some systematic features at the level of 1σ however appear as, mainly, a negative offset of the ACF for the $\ell 10$ maps. Indeed, we also observe this offset for the ACF of real data. We thus plot a gray region around the measured ACF to indicate the presence of this systematic.

3.2.2 Robustness to the cleaning procedure, Galactic model and masking

To test the robustness of our results with respect to the cleaning procedure ($\ell 1$ vs. $\ell 10$), Galactic model ($V1$ vs. $V2$) and Galactic mask ($|b| < 20^\circ, 30^\circ, 40^\circ, 50^\circ$ and Bubbles/Loop-I cut) we have computed the residuals of real Fermi maps using the different combinations of these procedures at all energy cuts. Then we have computed and compared the various ACFs and CCFs with all catalogs described in the following section. An example of these tests is shown in Fig. 3. The different panels show the ACF (left) and the

CCF with the CMB (right) relative to $V2$ model and $E > 3$ GeV cut. Top panels show the impact of the different cleaning procedures for the $V1$ galactic model. Middle panels are relative to the $V2$ galactic model. Bottom panels show the impact of different $|b|$ cuts.

The results of these tests can be summarized as the following: (i) for the ACF analysis the Galactic model $V2$ performs significantly better than $V1$ and therefore will be used throughout this work. (ii) The ACF is quite sensitive to different cleaning procedures and both the Bubbles/Loop-I mask and the $\ell 10$ cleaning are required to get consistent results. After this cleaning, the auto-correlation signal is stable for Galactic cuts $|b| \geq 20^\circ$. For these reasons, we will consider (and show) only the ACFs computed using the $V2$ model with $\ell 10$ cleaning, Bubbles/Loop-I mask and a Galactic cut $|b| = 20^\circ$. (iii) The CCFs are remarkably insensitive to cleaning procedures and masks already when using the $V1$ model, apart the case of no Bubbles/Loop-I mask and no $\ell 10$ cleaning which, not including any modeling of the Bubbles, leaves significant residuals which seem to bias the CCF result. Overall, this test show that the ACF and CCF signals converge to a stable result when progressively more aggressive cleaning procedures and latitude cuts are applied. For consistency with the ACF case we will consider (and show) the CCFs computed using the same Fermi-LAT maps used for the ACF analysis, although we did check for the robustness of all the CCFs with respect to the different cleaning procedures and masks.

3.2.3 Robustness to the event class type

A further check is performed comparing the ACF and CCFs previously obtained from *class 3* and *class 4* events maps with those computed from the *class 3* and *class 4* events together. In this second case the increased contamination from residual isotropic instrumental background is not expected to affect the CCFs although, of course, it can make the error bars slightly larger, which is indeed what was found. For the ACFs more effects come into play. For example, the enhanced isotropic instrumental component is expected to decrease the amplitude of the auto-correlation signal. However, since the measured ACF is consistent with zero, the only effect is, again, to slightly enlarge the error bars, which is indeed observed. Of course, the additional instrumental background associated to *class 3* events may not be completely isotropic. However, the fact that the measured ACF is consistent with that of the *class 4* events indicates that possible deviations from isotropy are too small to affect our analysis.

3.2.4 Sensitivity to the PSF of the detector

The angular resolution of the detector, characterized by its PSF, in principle introduces a correlation between neighboring pixels which may increase the auto-correlation signal on angular scales comparable with the PSF of the detector (causing the so-called *amplification bias*). The effect, however, is expected to be small since our bin-size is significantly larger than the original resolution of the maps. To estimate its impact on our analysis we have first computed the window function in multipole space associated to the PSF, given by $W_l(E) = \int d\theta P_l(\cos(\theta)) \text{PSF}(E, \theta)$, where $P_l(\cos(\theta))$ are the Legendre Polynomials and $\text{PSF}(E, \theta)$ is the energy dependent PSF. We have then multiplied W_l for the expected, intrinsic correlation given by Eq.8 and integrated back to configuration space. The result is shown in Fig. 4 in which we compare the expected intrinsic ACF (continuous, black curve) to that convolved with the

⁶ <http://fermi.gsfc.nasa.gov/ssc/data/access/lat/BackgroundModels.html>

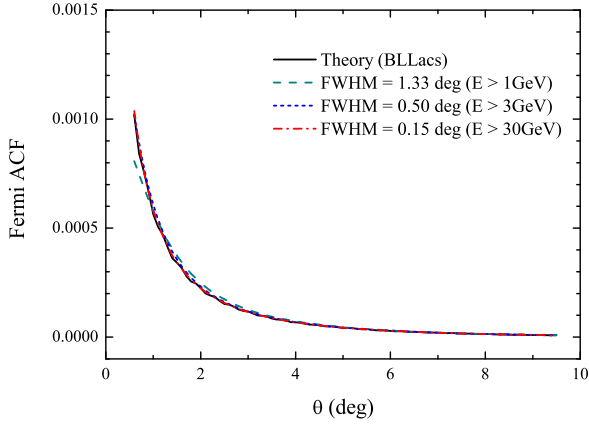


Figure 4. The effect of finite PSF on the ACF of BLLacs.

PSF at $E = 1$ GeV, 3 GeV, and 30 GeV which has a 68% containment radius of 0.8° (green, dot-dashed), 0.3° (blue, dotted), 0.1° (red, dashed) respectively (Atwood et al. 2009). Notice also that we compared the results with a simple Gaussian approximation for the window function, $W_l^2 = [\exp(-l^2\sigma_b^2/2)]^2$, where σ_b is the width of the beam, finding almost indistinguishable results. As can be seen, only for $E \geq 1$ GeV some small effects can be appreciated, while for $E > 3$ GeV this *amplification bias* is completely negligible.

3.2.5 Robustness to the event conversion type

As a further robustness test we also computed the ACF of those events labeled as *front* (Atwood et al. 2009) which are photons converting in the front part of the detector and have a significantly better PSF with respect to the rest of the events which, instead, convert in the back part of the detector where thicker converter foils increase the chance of large-angle scattering which deteriorates the tracking accuracy. They amount to about half of the events detected by the Fermi-LAT detector. We performed this test to check the robustness of the CCF with SDSS-LRGs and 2MASS galaxies in Sections 5.5 and 5.6, i.e. in the two cases in which we find some features in the CCFs. Apart from some increase in the error bars due to the halved statistics, the results did not change significantly.

3.3 WMAP7 ILC

In order to search for the ISW effect, we cross-correlate the Fermi-LAT 21-month EGB maps with the CMB maps derived from the 7-year WMAP data. More precisely, we use the WMAP Internal Linear Combination (ILC) map with $N_{\text{side}} = 512$ provided by the WMAP team (Komatsu et al. 2010), shown in Fig. 5. This ILC map was already built to minimize the Galactic and other foreground contaminations. For the WMAP map, we use the “KQ75” mask (Gold et al. 2010) corresponding roughly to the “Kp0” cut in the 3-year data release. In our calculations, we downgrade it to the resolution $N_{\text{side}} = 64$, to match that of the Fermi-LAT maps, and set the weight $w_T = 0$ for all pixels including at least one masked high resolution pixel (Raccanelli et al. 2008; Xia et al. 2009).

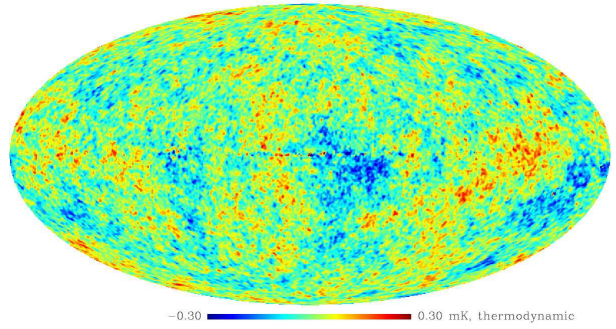


Figure 5. The 7-year WMAP ILC map in Galactic coordinates with the resolution $N_{\text{side}} = 512$.

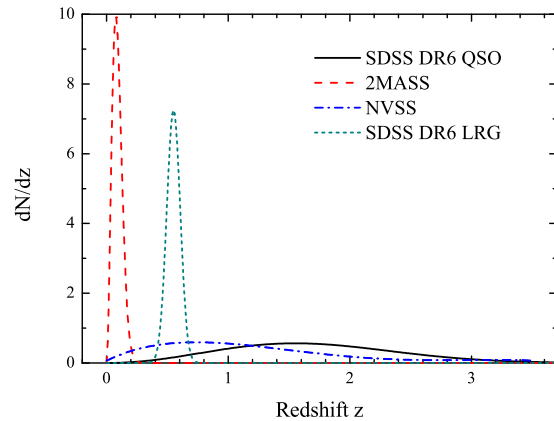


Figure 6. Normalized redshift distributions, dN/dz , of the different types of objects considered for our cross-correlation analysis. SDSS DR6 QSOs (black, continuous line), 2MASS galaxies (red, dashed), NVSS galaxies (blue, dot-dashed) and SDSS DR6 LRGs (cyan, short-dashed).

3.4 Discrete sources maps

One of our goals is to cross-correlate the EGB maps with different classes of sources that trace, but not necessarily coincide with, the EGB sources. Since all luminous objects trace, with a different degree of bias, the same underlying distribution of matter, it makes sense to cross correlate the EGB with the following sources: *i*) Optically selected quasars, *ii*) luminous radio galaxies, *iii*) IR-selected galaxies, and *iv*) LRGs. *(i)* and *(ii)* span the same, broad redshift range as the FSQRs whereas *(iii)* and *(iv)* span much narrower redshift ranges that overlap with those of BLLacs and Starforming galaxies. Below, we provide some details on the different catalogs considered in our analysis. In Fig.6 we show the redshift distribution, dN/dz , of the four catalogues we have considered in this paper. All distributions are normalized to unity. 2MASS galaxies and LRGs trace the large scale structure of the local universe and, from Fig. 1, we see that we can expect some cross-correlation signal only if the bulk of the EGB is contributed by star-forming galaxies or BLLacs. On the contrary, in the case of QSOs and NVSS galaxies, a positive cross-correlation may be expected if EGB were preferentially contributed by a population of high-redshift objects like FSQRs. However, the broad redshift distribution of these objects might also allow to pick up some cross-correlation signal provided by a population of low-redshift γ -ray sources.

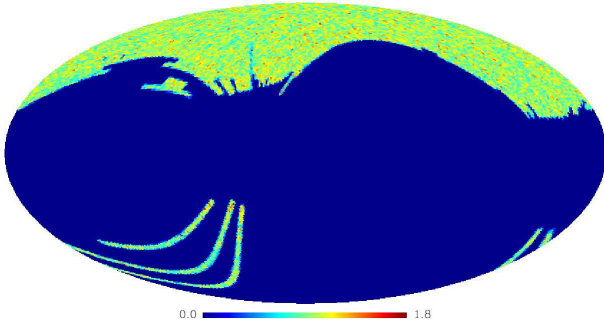


Figure 7. The number count map of SDSS DR6 quasar catalogue in Galactic coordinates with the resolution $N_{\text{side}} = 64$.

3.4.1 SDSS DR6 QSO

We use the SDSS DR6 quasar catalog released by Richards et al. (2009) (hereafter DR6-QSO). This catalog contains about $N_q \approx 10^6$ quasars with photometric redshifts between 0.065 and 6.075, covering almost all of the northern hemisphere of the Galaxy plus three narrow stripes in the southern, for a total area of 8417 deg^2 ($\sim 20\%$ of the area of the whole sky). The DR6-QSO data set extends previous similar SDSS data sets with $\sim 95\%$ efficiency (Richards et al. 2004; Myers et al. 2006). The main differences are due to the fact that DR6-QSO probes QSOs at higher redshift and also contains putative QSOs flagged as to have ultra violet excess (UVX objects). We refer the reader to Richards et al. (2009) for a very detailed description of the object selection with the non-parametric Bayesian classification kernel density estimator (NBC-KDE) algorithm.

We rely on the electronically published table that contains only objects with the “good” flag with values within the range $[0, 6]$. The higher the value, the more probable for the object to be a real QSO (Richards et al. 2009). We only consider the quasar candidates selected via the UV-excess-only criteria “uvxts=1”, i.e. objects clearly showing a UV excess which should be a signature of a QSO spectrum. We are left with $N_q \approx 6 \times 10^5$ quasars. In Fig. 7 we show the number counts map of the SDSS DR6 quasar catalogue in Galactic coordinates.

In order to determine the mask of the actual sky coverage of the DR6 survey, we generate a random sample with a sufficiently large number of galaxies using the DR6 database to ensure roughly uniform sampling on the SDSS CasJobs website. Following Xia et al. (2009), besides the pixel geometry mask, we also add the foreground mask by cutting the pixels with the g-band Galactic extinction $A_g \equiv 3.793 \times E(B - V) > 0.18$ to account for reddening that is the main systematic effect.

The redshift distribution function dN/dz of the DR6-QSO sample is approximated by the function:

$$\frac{dN}{dz}(z) = \frac{\beta}{\Gamma(\frac{m+1}{\beta})} \frac{z^m}{z_0^{m+1}} \exp\left[-\left(\frac{z}{z_0}\right)^\beta\right], \quad (12)$$

where three free parameters are $m = 2.00$, $\beta = 2.20$, and $z_0 = 1.62$ (Xia et al. 2009). We choose a constant bias $b_S = 2.3$ as found by Giannantonio et al. (2008); Xia et al. (2009) to calculate the theoretical prediction from the best-fit WMAP model adopted in this work.

3.4.2 2MASS

We use the 2 Micron All-Sky Survey (2MASS) extended source catalogue (Jarrett et al. 2000), which contains ~ 770000 galax-

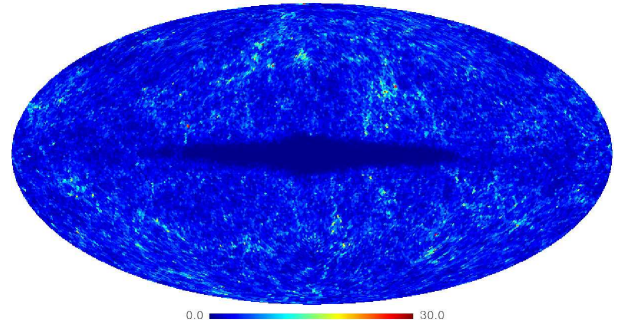


Figure 8. The number count map of 2MASS extended source catalogue in Galactic coordinates with the resolution $N_{\text{side}} = 64$.

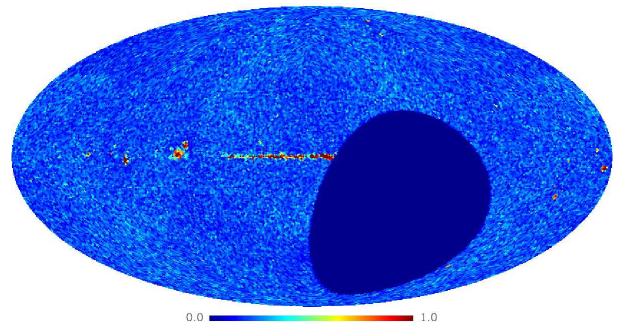


Figure 9. The number count map of NVSS radio sources in Galactic coordinates with the resolution $N_{\text{side}} = 64$.

ies with mean redshift $\langle z \rangle \approx 0.072$, as shown in Fig. 8. We select galaxies according to their K_s -band isophotal magnitude K_{20} , measured inside a circular isophote with surface brightness of 20 mag/arcsec^2 . These magnitudes are corrected for Galactic extinction using the infrared reddening maps: $K'_{20} = K_{20} - A_k$, where the extinction $A_k = 0.367 \times (B - V)$. In our analysis, we use the flux cut $12.0 < K'_{20} < 14.0$. We only include objects with a uniform detection threshold (`use_src = 1`), and remove known artifacts (`cc_flag \neq a` and `cc_flag \neq z`). Furthermore, we exclude areas of the sky with high reddening using the infrared reddening maps by Schlegel et al. (1998), discarding pixels with $A_k > 0.05$, which leaves approximately 67% of the sky unmasked.

In this case, the free parameters of the redshift distribution in Eq. 12 are $m = 1.90$, $\beta = 1.75$, and $z_0 = 0.07$ (Giannantonio et al. 2008), while as constant bias we use $b_S = 1.4$ as found by Rassat et al. (2007).

3.4.3 NVSS

The NRAO VLA Sky Survey (NVSS) (Condon et al. 1998) offers the most extensive sky coverage (82% of the sky to a completeness limit of about 3 mJy at 1.4 GHz) and contains 1.8×10^6 sources. Here, we include in our analysis only NVSS sources brighter than 10 mJy, since the surface density distribution of fainter sources suffers from declination-dependent fluctuations (Blake & Wall 2002). We also exclude the strip at $|b| < 5^\circ$, where the catalog may be substantially affected by Galactic emissions. The NVSS source surface density at this threshold is 16.9 deg^{-2} .

The redshift distribution at this flux limit has been recently determined by Brookes et al. (2008). Their sample, complete to a flux density of 7.2 mJy, comprises 110 sources with $S \geq 10 \text{ mJy}$,

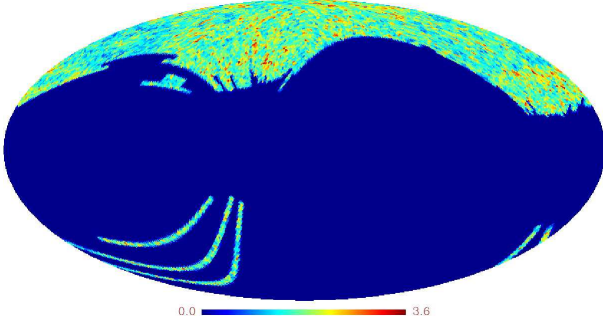


Figure 10. The number count map of MegaZ LRG catalogue in Galactic coordinates with the resolution $N_{\text{side}} = 64$.

of which 78 (71%) have spectroscopic redshifts, 23 have redshift estimates via the $K - z$ relation for radio sources, and 9 were not detected in the K -band and therefore have a lower limit to z . We adopt here the smooth description of this redshift distribution given by de Zotti et al. (2010):

$$\frac{dN}{dz}(z) = 1.29 + 32.37z - 32.89z^2 + 11.13z^3 - 1.25z^4. \quad (13)$$

Here, we simply use a constant bias $b_S = 1.5$ to calculate the theoretical prediction.

3.4.4 SDSS DR6 LRG

We use the updated MegaZ LRG sample (Abdalla et al. 2008), which contains $\sim 1.5 \times 10^6$ galaxies from the SDSS DR6 in the redshift range $0.4 < z < 0.7$ with limiting magnitude $i < 20$, as shown in Fig. 10. To reduce stellar contamination, there is a variable of the MegaZ neural network estimator δ_{sg} , defined such that $\delta_{\text{sg}} = 1$ if the object is a galaxy, and $\delta_{\text{sg}} = 0$ if it is a star. For a conservative analysis, we choose a cut $\delta_{\text{sg}} > 0.2$, which is reported to reduce stellar contamination below 2% while keeping 99.9% of the galaxies. In addition to the SDSS DR6 geometry mask, we also add two foreground masks to account for seeing (removing pixels with median seeing in the red band larger than 1.4 arcsec) and reddening (removing pixels with median extinction in the red band $A_r > 0.18$) (Giannantonio et al. 2008).

The redshift distribution function in this case is found directly from the photometric redshifts that are given in the catalogue (Collister et al. 2007), while we set the constant bias b_S to 1.8 (Giannantonio et al. 2008) when calculating the theoretical predictions.

4 CORRELATION ANALYSIS

In order to calculate the ACF and the CCF all maps have been rebinned to a resolution of $N_{\text{side}} = 64$. To estimate the ACF of the residual Fermi-LAT maps we use the following estimator $\hat{c}^{\text{ff}}(\theta)$:

$$\hat{c}^{\text{ff}}(\theta) = \frac{1}{\bar{n}^2 N_\theta} \sum_{i,j} (n_i - \bar{n})(n_j - \bar{n}), \quad (14)$$

where n_i is the number of γ -ray photons in each pixel and \bar{n} is the mean photon counts corresponding to the average EGB signal. The sum runs over all the pixels with a given angular separation. For each angular bin centered around θ , N_θ is the number of pixel pairs separated by an angle within that bin. The CMB maps consist of temperature difference maps. Therefore we replace the n_i and \bar{n}

with the temperature T_i in each pixel and the average temperature \bar{T} of the CMB map. The CCF estimator (in μK) between the Fermi-LAT map and the CMB temperature map $\hat{c}^{\text{fT}}(\theta)$ reads:

$$\hat{c}^{\text{fT}}(\theta) = \frac{1}{\bar{n} N_\theta} \sum_{i,j} (T_i - \bar{T})(n_j - \bar{n}). \quad (15)$$

Moreover, we are also interested in the cross-correlation between Fermi-LAT maps and the different maps of discrete sources. In this case, the CCF estimator is $\hat{c}^{\text{fg}}(\theta)$:

$$\hat{c}^{\text{fg}}(\theta) = \frac{1}{\bar{n} N_\theta} \sum_{i,j} (n_i^{\text{f}} - \bar{n}^{\text{f}}) \frac{(n_j^{\text{g}} - \bar{n}^{\text{g}})}{\bar{n}^{\text{g}}}. \quad (16)$$

Since we are using a resolution of $N_{\text{side}} = 64$, for which the pixel size is 0.92° , in our calculation we use $N_{\text{bin}} = 5$ linearly spaced angular bins in the range $1^\circ \leq \theta \leq 9^\circ$.

To compute the errors, we estimate the covariance matrix of the ACF (CCF) data points using jackknife resampling method (Scranton et al. 2002). This method divides the data into M patches, then M subsamples are created by neglecting each patch in turn. These patches have roughly equal area. In practice, we firstly list the whole set of pixels covered by the survey, and then divide them into $M = 30$ patches that do not have very similar shape, but have roughly equal area (i.e. equal number of pixels). The covariance estimator is:

$$C_{ij} = \frac{M-1}{M} \sum_{k=1}^M [\hat{C}_k(\theta_i) - \bar{C}(\theta_i)] [\hat{C}_k(\theta_j) - \bar{C}(\theta_j)], \quad (17)$$

where $\hat{C}_k(\theta_i)$ are the observed ACF (CCF) of the M subsamples in the i -th angular bin and $\bar{C}(\theta_i)$ are the mean ACF (CCF) over M realizations. The diagonal part of these matrices gives the variance of the ACF (CCF) in each bin $C_{ii}^k = \sigma_i^2$, while the off-diagonal part represents the covariance between the angular bins. We also change the number of patches M and verify that the covariance matrix is stable.

5 RESULTS

In this section we compute the ACF and the CCF of the different map combinations and compare the results with model predictions. The ACF signal could constrain the nature of the sources that contribute to the EGB. The presence of the ISW effect would quantify how well the EGB sources trace the underlying mass distribution and reveal the presence of a cosmological constant term. Finally, the strength of the CCF signal would indicate how closely a given class of objects trace the sources of the EGB. For each correlation analysis we will show measured quantities and theoretical predictions. The comparison between the two is only performed in configuration space, i.e. we over-plot the theoretical ACF and CCF (continuous curves) with the data points with error bars. In addition, we also will show mode predictions in Legendre space, i.e. through the expected angular power spectra, since this is the direct prediction of the model, and model to model comparison is easier in Legendre space. All theoretical predictions use Eq.8 to model the correlation between the γ -ray signal supposedly contributed by a single type of objects (FSRQs, BLLacs or Star forming galaxies) and a second fluctuation fields (the γ -ray background for the ACF, the CMB for the ISW signal and the discrete source catalogues for the cross-correlation analyses).

5.1 Auto-correlation analysis

In Fig. 11 we show the ACF of the residual maps obtained using the V2 Galactic model with $\ell 10$ cleaning, Bubbles/Loop-I masking and a Galactic cut $|b| = 20^\circ$. Different symbols indicate different energy cuts: black square is for $E > 1$ GeV, red dot is for $E > 3$ GeV and magenta triangle is for $E > 30$ GeV. Results for the $E > 30$ GeV case are shown in separate panel since the error bars are significantly larger. 1σ error bars were computed using the jackknife procedure. The three continuous curves in this plot and in all plots of the cross-correlation functions discussed in the following sections represent the theoretical predictions from Section 2.3 obtained assuming that each source class (BLLacs, FSRQs or Star Forming galaxies), specified by their luminosity density distribution $\rho_\gamma(z)$, contribute to a fraction of the EGB, f_j , listed in Table 1.

At small angular separations ($\theta < 2^\circ$) the auto-correlation signal is consistent with zero with all energy cuts but $E > 1$ GeV. Theoretical models do predict a weak auto-correlation signal at these angular separations that can be regarded as the typical angular size of the γ -ray emitting element. However, the predicted auto-correlation is much weaker than the measured one, at a level that would be indistinguishable from zero with the current uncertainties. Although a correlation signal at this level would still be possible from a contribution of unresolved point sources, we find that the signal is not very robust to the different cleaning methods and progressively disappears when we apply larger $|b|$ cuts. We therefore regard this as a spurious feature of the ACF at low energies where the Galactic contribution is stronger and its subtraction more prone to systematic errors. At larger separations ($\theta > 4^\circ$) the ACF is slightly negative. This is a spurious feature induced by the $\ell 10$ cleaning procedure as we have shown the Monte Carlo analysis presented in Section 3.2.1. The corrected signal would be consistent with zero. From the Monte Carlo we estimate that this systematic offset is at the level of the 1σ statistical error. We thus show in the plot also a systematic uncertainty band obtained doubling the 1σ statistical uncertainties.

To highlight the differences among the different source classes we plot the angular auto-power spectra in Fig. 12. BLLacs and star-forming galaxies have similar spectra, with more power on large scales than the FSRQ model. The situation is reversed at small scales. This difference simply reflects the fact that in the first two cases the γ -ray emission peaks at moderate redshifts $z = [0.5, 1]$ while for FSRQs the bulk of the γ -ray signal is produced at $z > 2$, as shown in Fig. 1. Since all models trace the same mass density field, i.e. assume the same $P(k)$, the power shift in Fig. 11 reflects the fact that the same physical scale is preferentially seen at different angles in the different models: large angles (small ℓ) for BLLacs and star-forming galaxies that typically sample the universe at low redshifts; small angles (large ℓ) for FSRQs that preferentially samples the universe at high redshifts. The larger amplitude of the spectrum for BLLacs to the spectrum of star-forming galaxies simply reflects the different bias factors of the two classes of objects.

5.2 ISW

In Fig. 13 we show the CCF of the EGB with the CMB, i.e. the ISW signal. The symbols refer to the CCF estimated from the 21-month Fermi-LAT maps and the WMP7 ILC map and the continuous lines represent model predictions. Different symbols indicate different energy cuts.

We note that the expected CCF signal is positive out to large angular separations and is only a factor 3-4 smaller than the width

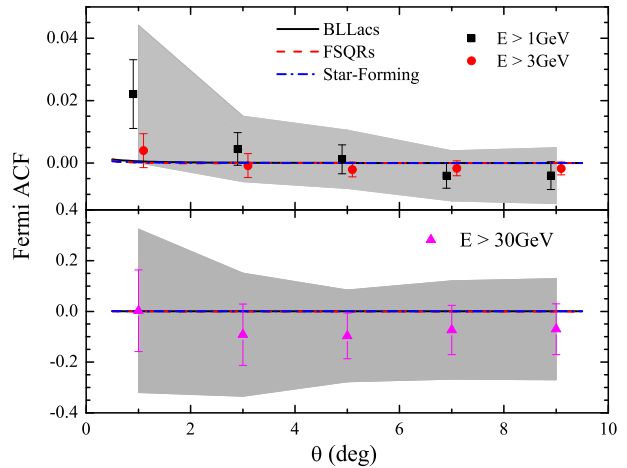


Figure 11. ACFs estimated from the 21-month Fermi-LAT EGB map for $|b| > 20^\circ$ in three energy bands: $E > 1$ GeV, $E > 3$ GeV (upper panel) and $E > 30$ GeV (below panel). Model predictions for different types of sources are represented by continuous curves: FSRQs (black, continuous), BLLacs (red, dashed) star-forming galaxies (blue, dot-dashed). The gray band indicates the systematic uncertainty coming from the foreground cleaning procedure estimated to be approximately equal to the 1σ statistical errors (see text). In the top panel only the band for the 1 GeV case is shown.

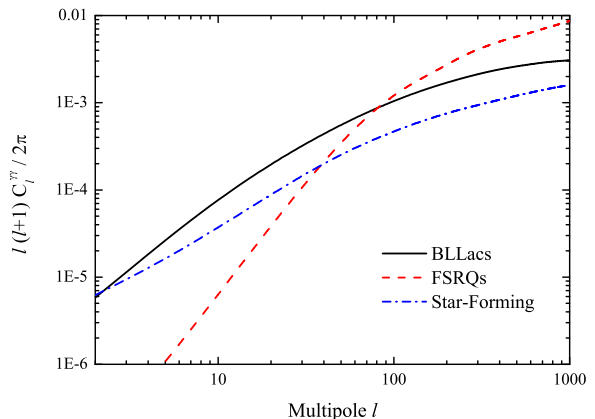


Figure 12. Angular auto-power spectra for different EGB source models. Different line-styles characterize different models. Black, continuous curve: FSRQs; red, dashed: BLLacs; blue, dot-dashed: star-forming galaxies.

of the error bars. This has to be compared with the ACF case where the expected signal is, instead, more than a factor of 10 smaller than the experimental error bars. This result, which reflects the better statistics of the CMB maps, indicates that the goal of detecting the ISW signature in the EGB is not unrealistic. However, with the limited statistics of the 21-month data the ISW signal is consistent with zero with all energy cuts. This (null) result is robust to different cleaning methods and latitude cuts.

From a theoretical point of view we notice that the ISW signal is expected to be larger in the BLLacs case than in the FSRQs one. This is because the former sample is rather local $z \leq 1$ and probes an epoch in which the cosmological constant drives the ac-

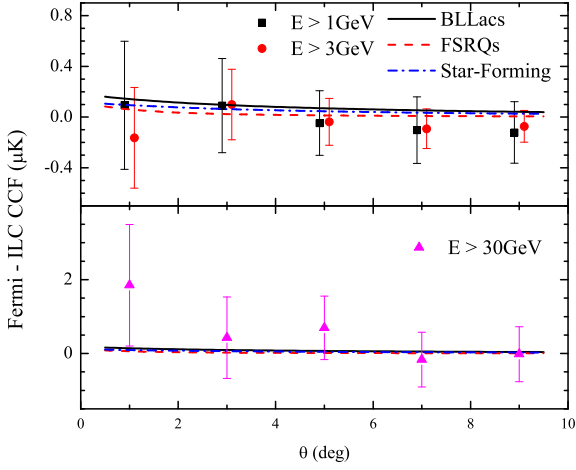


Figure 13. CCFs estimated from the WMAP7 ILC map and the 21-month Fermi-LAT EGB map with $|b| > 20^\circ$ in three energy bands. The three symbols refer to 3 energy cuts $E > 1$ GeV, $E > 3$ GeV (upper panel) and $E > 30$ GeV (below panel). Model predictions for different types of sources are represented by continuous curves: FSRQs (black, continuous), BLLacs (red, dashed), star-forming galaxies (blue, dot-dashed).

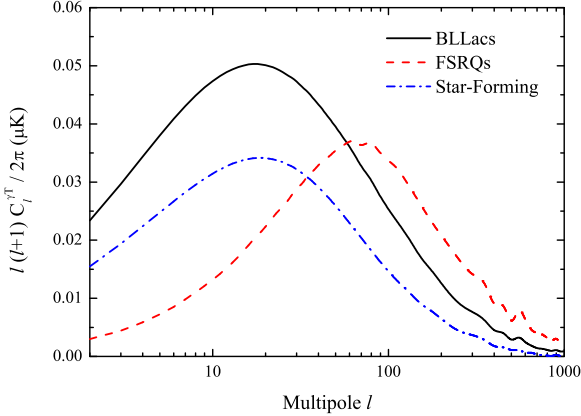


Figure 14. Angular cross-power spectra of the EGB with the CMB. Different line-styles characterize different models. Black, continuous curve: FSRQs. Red, dashed: BLLacs. Blue, dot-dashed: star-forming galaxies.

celerated expansion in which the late ISW effect sets in. FSRQs, instead, preferentially sample a high redshift, matter-dominated, flat universe from which we expect only a very weak ISW signature. Once again, the difference between the BLLacs and star-forming galaxies models reflects the different biases of the two populations. The difference among the models is best seen through their angular cross-spectra, shown in Fig. 14. As for the auto-power case, we notice that the FSRQs cross-power peaks at smaller angles than that of the other models, reflecting the different redshift sampled by the different classes of objects. The smaller power of the FSRQs model reflects the intrinsic weakness of the ISW signal, as anticipated. The drop at $l \sim 100$ is due to the late-time (low ℓ) nature of the ISW effect.

5.3 Cross-correlation with QSOs

In Fig. 15 we plot the estimated CCF between the Fermi-LAT EGB and the SDSS-DR6 QSOs maps compared with model predictions. Symbols and line-styles are the same as in Fig. 13. The expected CCF amplitude is rather weak. This is due to the quite sharp, high redshift peaks of the quasars' dN/dz which preferentially picks up the correlation signal from high redshifts. With a large z value, the $(1+z)^{-1}H^{-1}(z)$ dimming term in Eq. 9 weakens the correlation signal. The fact that the correlation signal comes from large redshift irrespective of the EGB model explored, is more clearly seen in Fig. 16 which shows that the angular power has indeed been driven toward small angular scales. We notice here that it is still physical to consider, for example, the star-forming galaxies model in relation to the cross-correlation with QSOs. Indeed, a cross-correlation analysis alone cannot unambiguously identify EGB sources since all of them trace, with different biases, the underlying Dark Matter field. So, there may be a positive cross-correlation with the SDSS-DR6 QSOs catalog, which hardly consists of star forming galaxies, even if the underlying sources of the EGB are star-forming galaxies, since both of them trace the Dark Matter field.

All CCFs are consistent with zero. The weak ($\sim 1\sigma$) positive correlation in the innermost bin for the $E > 3$ GeV case (which would be consistent with theoretical expectations), disappears for the different choices of the cleaning method and/or when increasing the $|b|$ cut.

Note that, although the SDSS DR6 QSO catalog has very high efficiency in the selection algorithm, stars are point-like sources that inevitably contaminate the catalog. To compute the stellar contamination, we extract a large number ($\sim 8 \times 10^4$) of stars from the SDSS DR6 survey in the magnitude range $16.9 < g < 17.1$ using the CasJobs⁷ website and compute the CCF between stars and the Fermi maps $\hat{c}^{\text{fs}}(\theta)$. We have carefully checked that the contribution from contaminating stars to the CCF between QSOs and Fermi-LAT maps is fully consistent with zero and can safely be neglected.

5.4 Cross-correlation with NVSS galaxies

The dN/dz of NVSS galaxies peaks at lower redshifts than the QSO ones. For this reason the expected CCF signal is larger than for QSOs (see Fig. 17) and the cross-power shifts at larger angles (see Fig. 18). FSRQs have a weaker cross-correlation signal (and cross-power) because there is little overlap between the NVSS dN/dz and the redshift distribution of the γ -ray emission signal (see Fig. 1).

The estimated CCFs are consistent with zero and with theoretical predictions, despite the fact that all Fermi sources, including normal galaxies, are also NVSS sources. At the moment, this result is not worrisome given that the expected signal still fits within the large error bars. It will be indeed interesting to see if it persists with larger statistics.

5.5 Cross-correlation with LRGs galaxies

Fig. 19 shows that the expected amplitude of the CCF with the LRGs for BLLacs and star-forming galaxies is larger than that of NVSS galaxies because the LRGs distribution peaks at similar scales but is much sharper. As a consequence the peak of the angular cross-power for BLLacs and star-forming galaxies is quite similar to the NVSS one with some more power at small angles (see

⁷ <http://casjobs.sdss.org/dr7/en/>

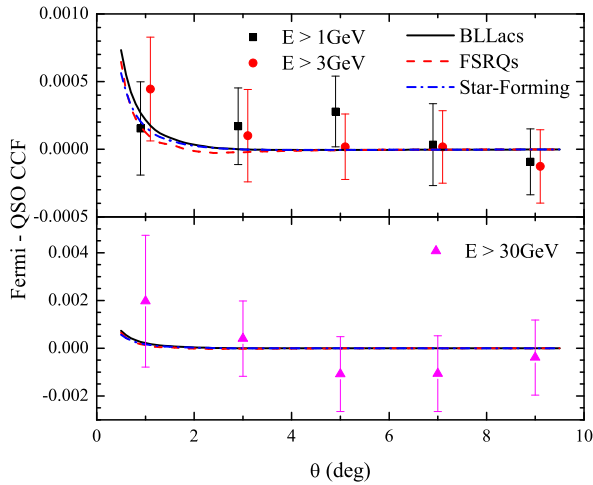


Figure 15. CCFs estimated from the SDSS DR6 QSO map and the 21-month Fermi-LAT EGB map with $|b| > 20^\circ$ in three energy bands. The three symbols refer to 3 energy cuts $E > 1$ GeV, $E > 3$ GeV (upper panel) and $E > 30$ GeV (below panel). Model predictions for different types of sources are represented by continuous curves: FSRQs (black, continuous), BLLacs (red, dashed) star-forming galaxies (blue, dot-dashed).

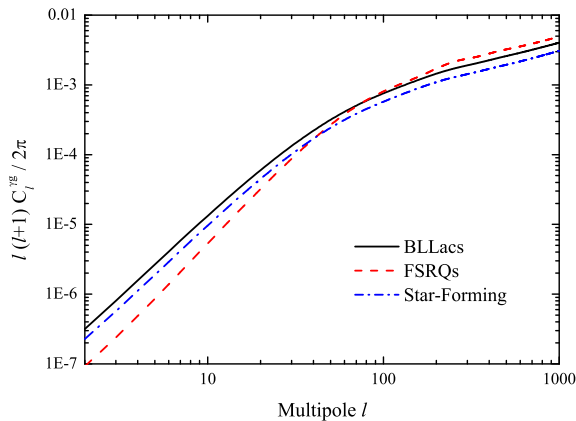


Figure 16. Angular cross-power spectra of the EGB with the SDSS-DR6 QSOs. Different line-styles characterize different models. Black, continuous curve: FSRQs. Red, dashed: BLLacs. Blue, dot-dashed: star-forming galaxies.

Fig. 20). There is no curve for the FSRQs case since this model predicts zero cross-correlation signal because there is no overlap between the dN/dz distribution of the LRGs and the predicted redshift distribution of γ -ray signal.

The measured CCFs is consistent with zero for $E > 3$ and $E > 30$ GeV. With the lowest energy cut, $E > 1$ GeV, we detect a positive correlation signal at $\theta < 2^\circ$ at $\sim 2\sigma$ confidence. This signal is remarkably robust to cleaning procedures and Galactic cuts. This feature is also robust to the choice of the γ -ray events since it is also present when we only consider the so-called front γ -ray photons which have a significantly better PSF.

Theoretical predictions agree with this signal at the $\sim 1.5\sigma$ level. The fact that is only seen at low energies may indicate that

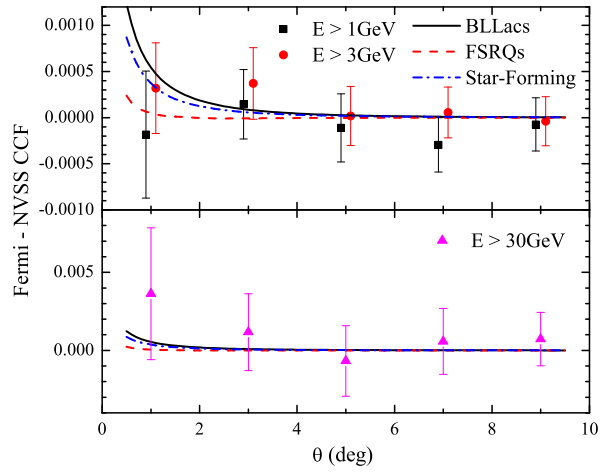


Figure 17. CCFs estimated from the NVSS galaxies map and the 21-month Fermi-LAT EGB map with $|b| > 20^\circ$ in three energy bands. The three symbols refer to 3 energy cuts $E > 1$ GeV, $E > 3$ GeV (upper panel) and $E > 30$ GeV (below panel). Model predictions for different types of sources are represented by continuous curves: FSRQs (black, continuous), BLLacs (red, dashed) star-forming galaxies (blue, dot-dashed).

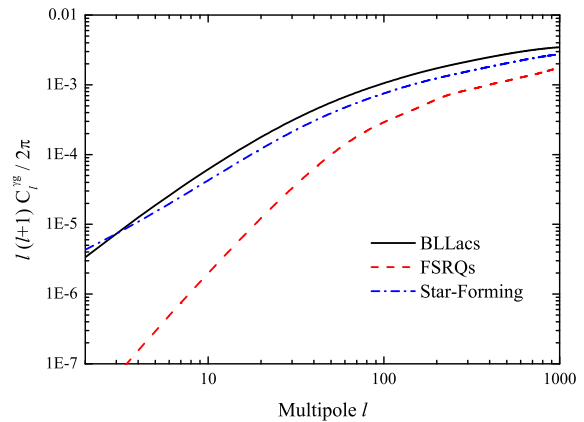


Figure 18. Angular cross-power spectra of the EGB with the NVSS galaxies. Different line-styles characterize different models. Black, continuous curve: FSRQs. Red, dashed: BLLacs. Blue, dot-dashed: star-forming galaxies.

the sources that contribute to the EGB at low energies are brighter than expected in our power-law model, i.e. the bias of the EGB sources (b_γ in Eq.9) is larger than expected. More intriguingly, this may indicate that there is a transition in energy in the sources contributing to the EGB from e.g. galaxies or BLLacs at low energy (which cross-correlate with LRGs) to FSRQs at high energies (which do not).

A further alternative is that this signal may come from the cross-correlation with the γ -rays contributed by sources coincident with LRGs but that are still too faint to be detected. Luckily, more statistics and better understanding of the diffuse foregrounds will help in the near future to better characterize this feature (for example using finer angular bins or lower energy photons) and check the validity of the previous hypotheses.

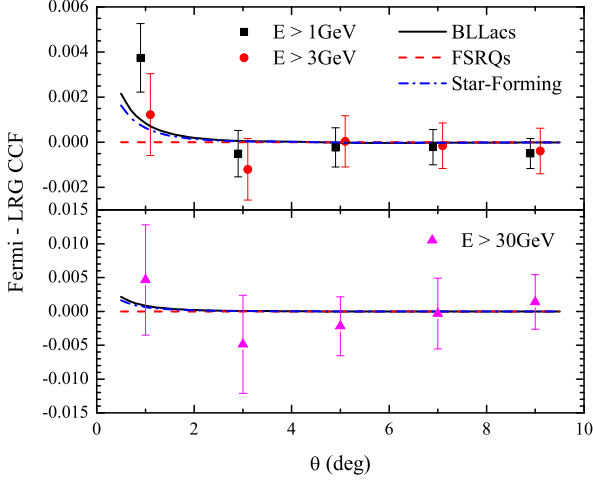


Figure 19. CCFs estimated from the LRGs map and the 21-month Fermi-LAT EGB map with $|b| > 20^\circ$ in three energy bands. The three symbols refer to 3 energy cuts $E > 1$ GeV, $E > 3$ GeV (upper panel) and $E > 30$ GeV (below panel). Model predictions for different types of sources are represented by continuous curves: FSRQs (black, continuous), BLLacs (red, dashed), star-forming galaxies (blue, dot-dashed).

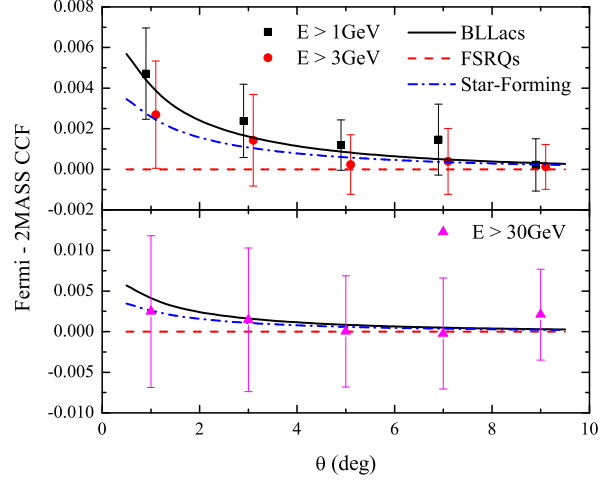


Figure 21. CCFs estimated from the 2MASS map and the 21-month Fermi-LAT EGB map with $|b| > 20^\circ$ in three energy bands. The three symbols refer to 3 energy cuts $E > 1$ GeV, $E > 3$ GeV (upper panel) and $E > 30$ GeV (below panel). Model predictions for different types of sources are represented by continuous curves: FSRQs (black, continuous), BLLacs (red, dashed) star-forming galaxies (blue, dot-dashed).

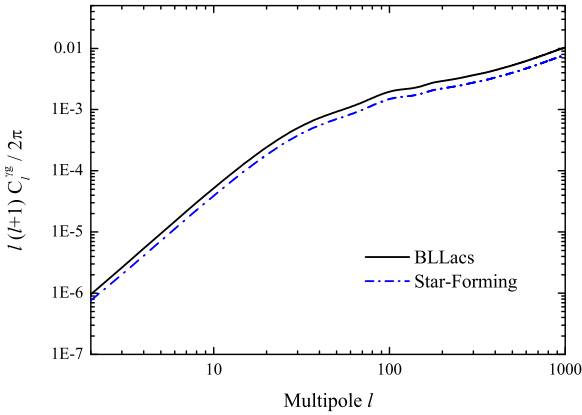


Figure 20. Angular cross-power spectra of the EGB with the LRGs. Different line-styles characterize different models. Black, continuous curve: BLLacs. Blue, dot-dashed: star-forming galaxies.

5.6 Cross-correlation with 2MASS galaxies

The result of the cross-correlation between Fermi-LAT EGB maps and 2MASS catalog (that represents the most local of our samples) confirms the trend of the other cross-correlation analyses: increase of the expected CCF amplitude predicted by the models of BLLacs and star-forming galaxies (see Fig. 21), angular power that shifts toward larger angles (see Fig. 22) and zero correlation expected for an EGB solely contributed by FSRQs. We note that, as expected, the theoretical angular cross-spectrum is in good agreement with the one computed by Ando & Pavlidou (2009). The small differences likely arise from the fact that in our estimate we did not account for the angular resolution of the instrument and did not filter the angular power spectrum accordingly.

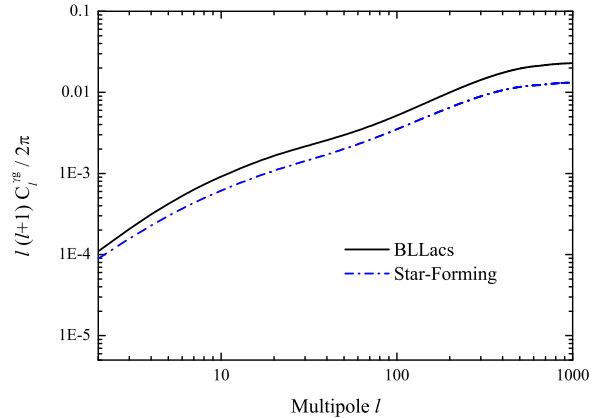


Figure 22. Angular cross-power spectra of the EGB with the 2MASS galaxies. Different line-styles characterize different models. Black, continuous curve: BLLacs. Blue, dot-dashed: star-forming galaxies.

The measured cross-correlation signal is consistent with zero at all but small angular separations and for $E > 1$ GeV, where we detect a hint of positive correlation. However, the reality of this correlation signal is questionable for two reasons. On one side, we found that this signal is rather sensitive to the cleaning procedure and to the Galactic mask adopted. Also in the LRGs case we made a further check using `FRONT` events only, but the sensitivity to data cleaning technique still persists. On the other side, this signal could be related to some possible systematic errors in the treatment of the 2MASS catalogue which has been advocated to settle some controversy in the ISW detection (Francis & Peacock 2010).

Table 2. χ^2 test of the observed data against the Λ CDM and SCDM models.

Sources	Current Data (χ^2)		Forecast ($\Delta\chi^2$)	
	Λ CDM	SCDM	Five years	Ten years
FSRQs	19.94	20.33	0.7	1.3
BLLacs	19.21	19.45	0.6	1.2
Star-form.	20.80	21.50	1.8	3.5

6 ANALYSIS

In this section we quantify the capability of the correlation analyses presented in the previous sections to constrain the cosmological model and the nature of the sources that contribute to the EGB using the observed ACFs and CCFs. For this purpose we only consider $E > 3$ GeV maps that allowed to obtain robust results (in contrast with the $E > 1$ GeV case) with reasonable errorbars (in contrast with the $E > 30$ GeV case).

To do this we have computed the following χ^2 function:

$$\chi^2 = \sum_{i,j,k,l} C_{i,j,k,l}^{-1} (d_i^{\gamma,k} - t_i^{\gamma,k})(d_j^{\gamma,l} - t_j^{\gamma,l}), \quad (18)$$

where $d^{\gamma,k}$ represents the measured CCF between the diffuse EGB and the catalog k (coinciding with the ACFs when $k = \gamma$) and $t^{\gamma,k}$ is the theoretical prediction. The i, j indexes run over the 5 angular bins of each of the various ACF/CCFs, while the k, l indexes run over the different ACF/CCFs. $C_{i,j,k,l}$ indicates the general covariance matrix obtained from the jackknife resampling, and contains the correlation between different angular bins as well as between the various ACF/CCFs relative to different catalogues. In practice, this χ^2 statistics compares the measured ACF and CCFs presented in Section 5 for our 3 model predictions (BLLacs, FSRQs and star-forming galaxies), considering all angular separations $\theta \leq 10^\circ$ and taking into account the covariance among the different ACF/CCF estimates.

The purpose of this comparison is twofold. First, we want to check whether this analysis is sensitive to the presence of a cosmological constant (mainly through the EGB - CMB comparison). Second, within a given cosmological framework, we want to check our ability of discriminating among competing models for the EGB. To answer these questions we have performed two different tests.

The results of the first test are summarized in Table 2. Columns 2 and 3 list the χ^2 values obtained when we consider the ‘‘concordance’’ Λ CDM model adopted in this paper (second column) and the χ^2 values obtained when we consider a CDM Einstein-de Sitter model with $\Omega_m = 1.0$ (SCDM, third column). The different rows refer to the three EGB models considered (column 1). The χ^2 values obtained for the two cosmological models are rather small. This similarity reflects the insensitivity of our correlation analysis to the presence of a cosmological constant term. The situation will improve significantly with the future Fermi-LAT data. In columns 4 and 5 we list the increase of the χ^2 , relative to the values in column 2, expected after $t_{\text{obs}} = 5$ and $t_{\text{obs}} = 10$ years of observations, respectively. This forecast has been obtained by assuming Poisson errors i.e. by scaling the 21-month errorbars by $\sqrt{t_{\text{obs}}}$. One can see that with $t_{\text{obs}} = 10$ years one expects to discriminate a Λ CDM model from a SCDM scenario at about 2σ confidence level if the EGB were mainly contributed by star-forming galaxies. This estimate assumes Gaussian statistics and refers to the

case of one free parameter only: the value of Ω_m . In fact the situation is likely to be more favorable since future data will also allow to improve the Galactic foreground model. In this way we will be able to extend the correlation analyses to lower energy bands. In addition, one can improve the effectiveness of the χ^2 statistics by carefully selecting the range of angular scales to be considered or by restricting the analysis to a few CCFs, among which the CCF with the CMB will play a crucial role since, as we have pointed out, the ISW signal is very sensitive to the underlying cosmological model.

As a second test we have computed the χ^2 varying the fraction of objects that contribute to the EGB, f_j , in the interval $[0,1]$. In this case we do not use the values listed in Table 1 but let the contribution of each source type vary between 0% to 100%. As before, we do not explore the case of a mixed contribution from different types of sources. The sensitivity to f_j comes, in this case, entirely from the linear dependence of the normalization of ACFs and CCFs on f_j itself. We note that varying f_j would affect the prediction for the γ -ray flux as a function of redshift. We decided to neglect this effect given the large uncertainties in the modeling of the sources. The results are displayed in Fig. 23. The plots show the χ^2 as a function of the EGB fraction contributed by the source f_j . The three panels refer to the three models explored: FSRQs, BLLacs and star-forming galaxies and, within each panel, the three curves refer to different observation times: 21 months (continuous, black), 5 years (dashed, red) and 10 years (dot-dashed, blue). The vertical lines are drawn in correspondence of the reference values of f_j listed in Table 1. The minima of the χ^2 do not coincide with the fiducial values for f_j . However, with the current 21-month data the discrepancy is hardly significant (barely above $1\text{-}\sigma$ in the BLLacs model). We note that if one removes the physical constraint $f_j \leq 1$ then for the FSRQs the minimum of the χ^2 would be found at $f_j > 1$. The fact that FSRQs favor large values of f_j is not surprising. It simply reflects the fact that their γ -ray flux is preferentially produced at large redshifts (see Fig. 1) and, as a consequence, that all their angular spectra plotted in Section 5 have smaller amplitudes than in the BLLacs and Star Forming galaxy cases. Notice, however, that overall the sensitivity to the FSRQs component is very weak and it is not expected to provide significant constraints even after 10 years of data taking. The constraints will improve significantly with the future Fermi-LAT maps: in the case of BLLacs and star-forming galaxies, after 10 years of data taking one would be able to reject the hypothesis of 100% contribution to the EGB at the $\gtrsim 3\sigma$ confidence level (but only to $\sim 1.5\sigma$ for the FSRQs).

7 DISCUSSION

The results presented in Section 5 show that with the current uncertainties it is not possible to discriminate among the different models of source populations, considered in this paper, contributing to the EGB emission. The measured ACF and CCFs are generally consistent with zero and, in particular, the lack of a measurable ISW effect prevents us from inferring the presence of a cosmological constant. The χ^2 test presented in Section 6, however, demonstrates that the situation will improve with the duration of the Fermi-LAT mission that, thanks to the sheer number of the collected photons, will allow to reduce the Poisson noise that contribute to the total uncertainties.

However, it is worth pointing out that, at present, the main factor limiting the correlation analyses is not photon counts statistics but the imperfect knowledge of the diffuse Galactic background which prevents us from using the data at very low Galactic lati-

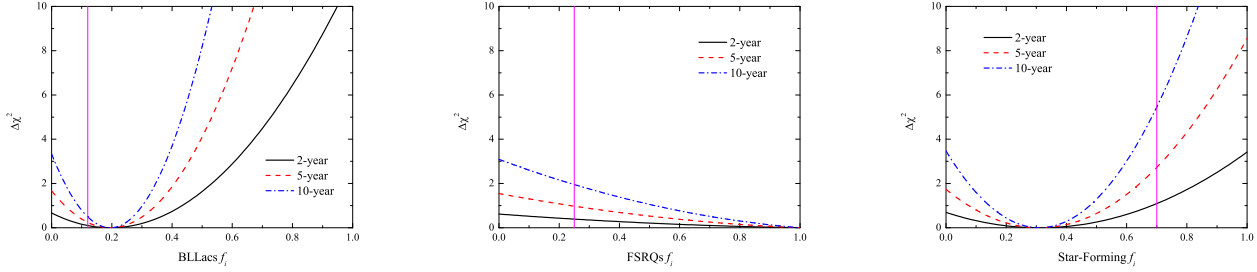


Figure 23. Limits on the fraction of three possible EGB sources from the current 21-month Fermi-LAT data (black, continuous) and the future 5-year (red, dashed), 10-year (blue, dot-dashed) Fermi-LAT observations. The vertical lines denote the maximum values of fractions from the current theoretical constraints.

tude and, especially, in the lower energy band. Clues that on some scales the current Galactic diffuse emission is not perfectly modeled are found when we compute the ACF and when we cross-correlate the 2MASS galaxy and the QSO-SDSS catalogs with the residual Fermi-LAT maps obtained with the lowest energy threshold $E > 1$ GeV. In those cases we did find a weak correlation signal at small angular separation $\theta \leq 2^\circ$ that, however, is very sensitive to the cleaning procedure and that disappears when a progressively larger strip across the Galactic plane is excluded from the analysis. A more convincing correlation signal is detected at the same separations and energy threshold when we cross-correlate the Fermi-LAT maps with the distribution of the SDSS LRGs. This signal is remarkably robust to masking and cleaning procedures. However this signal is above theoretical expectations and is only detected at low energy. If genuine, a positive cross correlation signal indicates that sources contributing to the EGB are traced by LRGs and prompts some further speculations. The fact that at $E \sim 1$ GeV the measured signal is larger than expected may indicate that, at this energy, the bias of the EGB sources (b_γ in Eq.9) is larger than expected. In addition, the fact that the cross-correlation signal drops for $E > 3$ GeV may suggest that EGB is not contributed by a single type of objects. Instead, the EGB would be produced by different types of sources and their relative contributions depend on energy. In this particular case, the decrease at $E = 3$ GeV could indicate that the relative contribution of FSRQs, whose cross-correlation with LRGs is expected to be zero, increase with energy. Another possibility is that the γ -rays are physically associated to LRGs just below the Fermi-LAT detection threshold.

The model of Galactic diffuse emission is expected to improve in the near term, when future dedicated analyses, based on a better photon statistics, will be available. As a result it will be possible to confirm or disprove these correlation signals and the validity of the above speculations. Moreover, improving the Galactic model will significantly increase photon statistics by extending the correlation analysis to lower energy bands.

The actual reduction of the error bars will be more severe than what expected from simple statistics since a larger sky coverage will allow to sample new structures, effectively reducing the Cosmic Variance. Future cross-correlation studies will also benefit from planned galaxy redshift surveys like EUCLID (Laureijs 2009), JDEM (Gehrels 2010) and Big Boss (Schlegel et al. 2009) that will be able to trace the large scale structure over a large fraction of the sky probing the crucial epoch in which the current accelerated expansion of the Universe has presumably started.

The main aim of the χ^2 tests presented in Section 6 was to illustrate the limitations of the correlation analysis of the current datasets and to show that future datasets will probably allow to

marginally detect the EGB correlation signal and the ISW effect. Another way to improve the statistical significance of the future detections is to optimize the tools to compare model with data and to consider additional objects' catalogs in the cross-correlation analysis. Exploring the potential of the various statistical tools that could be employed in a cross-correlation analysis is beyond the scope of this paper. However, even with the paradigmatic case of the χ^2 statistics, significant improvement can be obtained by restricting the comparison to some particular range of angular scales, energy range or to some particular catalogs of objects. From a more general perspective, the most rewarding way of extracting astrophysical and cosmological information from the diffuse EGB is to perform a combined likelihood analysis combining the cross-correlation analyses presented in this work with the one-point statistics, angular auto-correlation and spectral information, as suggested by Dodelson et al. (2009).

We stress that the EGB models used in this paper can and will improve significantly in the near future. Indeed, the number of resolved extragalactic sources is bound to increase with time. On one hand, this will allow us to resolve an increasing fraction of the diffuse EGB. On the other hand, the next generation catalogs of extragalactic source will allow to probe more reliably the faint end of the $\log N$ - $\log S$ of blazars and will provide better and better estimates of their contribution to the diffuse EGB. Population studies with higher statistics will also likely result in the detection of the expected break in the luminosity function, allowing to drop the assumption of a minimum L_{MIN} . With strong constraints on the blazars' contribution, one could afford exploring the case of mixed contribution from different types of sources, especially if the analysis can be performed over an extended range of energies, since the contribution from star-forming galaxy is expected to increase below 1 GeV. In this context one may also include the possible γ -ray photons from DM annihilation in extragalactic halos, whose contribution to the EGB has been modeled by several authors (e.g. Ullio et al. (2002); Ando (2005); Pieri et al. (2009)).

Finally, it is worth pointing out that investigating the ISW effect using γ -ray data (even if on its own it does not provide tight constraints on the cosmological parameters) is of considerable importance since it would represent a consistency check for the Λ CDM model obtained from a new, independent dataset. Current ISW estimates that rely on different tracers for large scale structure are sometimes in tension with the amplitude value for a Λ CDM model (e.g. Ho et al. (2008)). The new analysis performed in this paper can contribute to quantify to what extent such measurements are reliable and identify possible systematic effects.

8 SUMMARY AND CONCLUSION

In this work we have extracted the maps of the diffuse EGB from the 21-month Fermi-LAT data by masking γ -ray point sources from the Fermi-LAT data and by subtracting the various available models of the Galactic diffuse signal.

These residual sky maps have been used to compute the angular two-point auto-correlation function of the diffuse signal. To minimize possible systematic effects that may affect the correlation analysis, we have thoroughly checked for the presence of spurious signals due to an imperfectly subtraction of the Galactic foreground. In practice, we have tested the robustness of all measured ACFs and CCFs to Galactic foreground models, cleaning procedures and masking strategies. In doing so we have optimized a strategy with combined cleaning and masking procedures that allows to reduce systematic uncertainties. We note that, as expected, the ACF is much more prone to systematic effects than the CCF which, by contrast, is remarkably stable.

In addition to the auto-correlation analysis, complementary to the recent determination of the Fermi-LAT angular power spectrum by Gomez Vargas et al. (2010) and by Siegal-Gaskins et al. (2010), we have cross-correlated these EGB maps with the WMAP7 CMB map, in an attempt to detect the ISW effect. Finally, to unveil the nature of the unresolved sources that may contribute to the EGB we have cross-correlated the Fermi-LAT EGB maps with the angular distribution of different types of extragalactic objects in several catalogs. More specifically we have considered the local population of 2MASS galaxies, that should trace the EGB contribution from star-forming galaxies, and the more distant population of LRGs, NVSS radio galaxies and QSOs that may trace the population of blazars.

All the measured ACFs and CCFs have been compared with theoretical predictions in which the mean EGB signal and its angular correlation properties have been modeled assuming only one type of contributing sources: star-forming galaxies, BLLacs or FSRQs. The results of these comparisons allow, in principle, to constrain the level of contribution to the EGB of the different sources and, mainly through the ISW signal, the value of Ω_Λ .

The main results of our analysis can be summarized as follows:

- The measured ACF of the EGB above 3 GeV is consistent with zero at all angular separations. This result is in agreement, within the large error bars, with theoretical predictions since the auto-correlation signal is expected to be very small in all EGB models explored in this work. In other words, the auto-correlation function does not seem to be the best statistical tool to reveal the nature of the sources that contribute to the EGB. In the $E > 1$ GeV band we detect a $\sim 2\sigma$ positive correlation signal at $\theta \leq 2^\circ$ which, however, disappears when we increase the size of the Galactic mask. Considering the sensitivity of the ACF analysis on the Galactic diffuse model, especially at low energy, we conclude that this signal is a spurious feature.
- The measured ISW signal in the energy band is also consistent with zero at all energies. The expected amplitude, however, is significantly larger than that of the auto-correlation signal, suggesting that future data with better photon statistics and more accurate subtraction of the Galactic contribution could allow one to detect the ISW signature.
- The CCFs measured considering various objects catalogs are generally consistent with zero with a couple of exceptions: SDSS QSOs and 2MASS galaxies show a positive cross-correlation signal with the $E > 1$ GeV Fermi-LAT photons for $\theta \leq 2^\circ$. However, neither signal is robust to the cleaning procedure and the Galac-

tic mask applied. A more intriguing correlation signal is found at these same separations and energy when we correlate the Fermi-LAT maps with the SDSS LRGs. Unlike the previous cases, this signal, which is detected at 2σ , is remarkably robust to the model adopted for the Galactic diffuse signal, to the procedure to clean out spurious residuals and to the size and shape of the mask applied to exclude the Galactic plane and the Bubble/Loop-I regions. The analysis of future Fermi-LAT data will clarify the reliability and the nature of all these features.

- A simple χ^2 test performed using all the measured correlation functions confirms, in a more quantitative way, that 21-month Fermi-LAT maps allow to neither investigate the nature of the EGB nor constrain the value of the cosmological constant. However, this analysis shows that 10-year Fermi-LAT data would allow to constrain the contribution of star-forming galaxies of BLLacs to the EGB with a confidence level of $\gtrsim 3\sigma$ and to confirm the presence of a cosmological constant with a statistical significance of $\sim 2\sigma$.
- These estimates are very conservative since they are based on a simple extrapolation of the 21-month data assuming pure Poisson errors. The Galactic diffuse model, however, is likely expected to improve in the near future, while, new Fermi-LAT data will allow to better constrain the contribution to the EGB of some extragalactic objects like the FSRQs and the BLLacs. As a result, we will be able to extend the CCF analysis to lower energies, further improving the photon statistics, and providing more secure priors for the χ^2 analysis.

ACKNOWLEDGMENTS

AC, EB and MF thank the Institute of Theoretical Physics, University of Zurich and the Center for Cosmology and Astro-Particle Physics of The Ohio State University for the kind hospitality. Their visits were partially supported by NASA through the Fermi GI Program grant number NNX09AT74G. MF thanks the support of the Spanish MICINN's Consolider-Ingenio 2010 Programme under grant MultiDark CSD2009-00064. MV is supported by INFN-PD51, ASI/AAE contract, a PRIN MIUR, a PRIN INAF and the FP7 ERC starting grant "cosmolIGM".

We would like to thank M. Ajello and M. Ackermann for carefully reviewing the manuscript and providing comments and suggestions which have contributed to sensibly improve the analysis. In particular, we thank M. Ajello for kindly providing the Monte-carlo simulation of the population of Blazars which we have used to validate the analysis.

The Fermi LAT Collaboration acknowledges generous ongoing support from a number of agencies and institutes that have supported both the development and the operation of the LAT as well as scientific data analysis. These include the National Aeronautics and Space Administration and the Department of Energy in the United States, the Commissariat à l'Énergie Atomique and the Centre National de la Recherche Scientifique / Institut National de Physique Nucléaire et de Physique des Particules in France, the Agenzia Spaziale Italiana and the Istituto Nazionale di Fisica Nucleare in Italy, the Ministry of Education, Culture, Sports, Science and Technology (MEXT), High Energy Accelerator Research Organization (KEK) and Japan Aerospace Exploration Agency (JAXA) in Japan, and the K. A. Wallenberg Foundation, the Swedish Research Council and the Swedish National Space Board in Sweden.

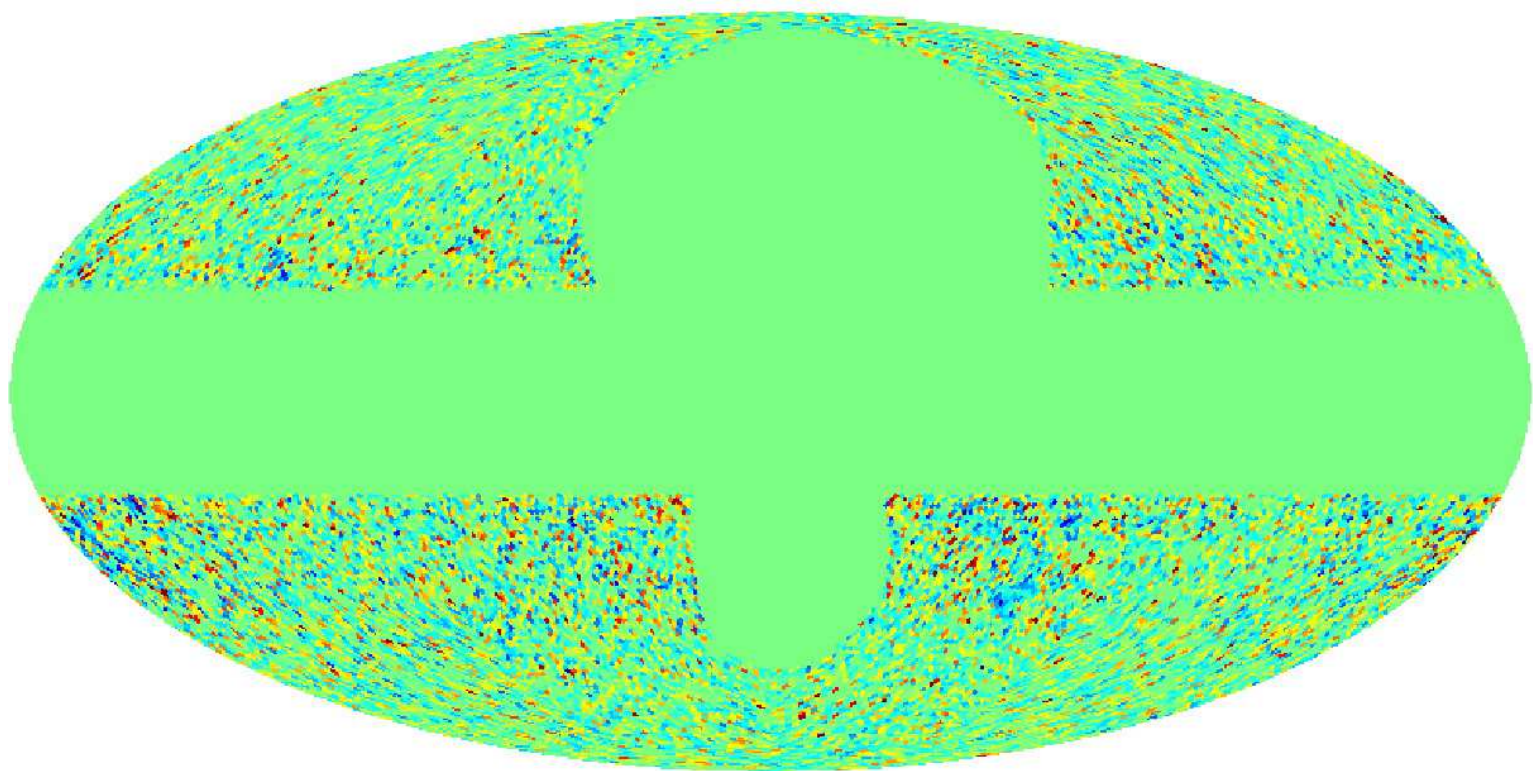
Additional support for science analysis during the operations phase is gratefully acknowledged from the Istituto Nazionale di

Astrofisica in Italy and the Centre National d'Études Spatiales in France.

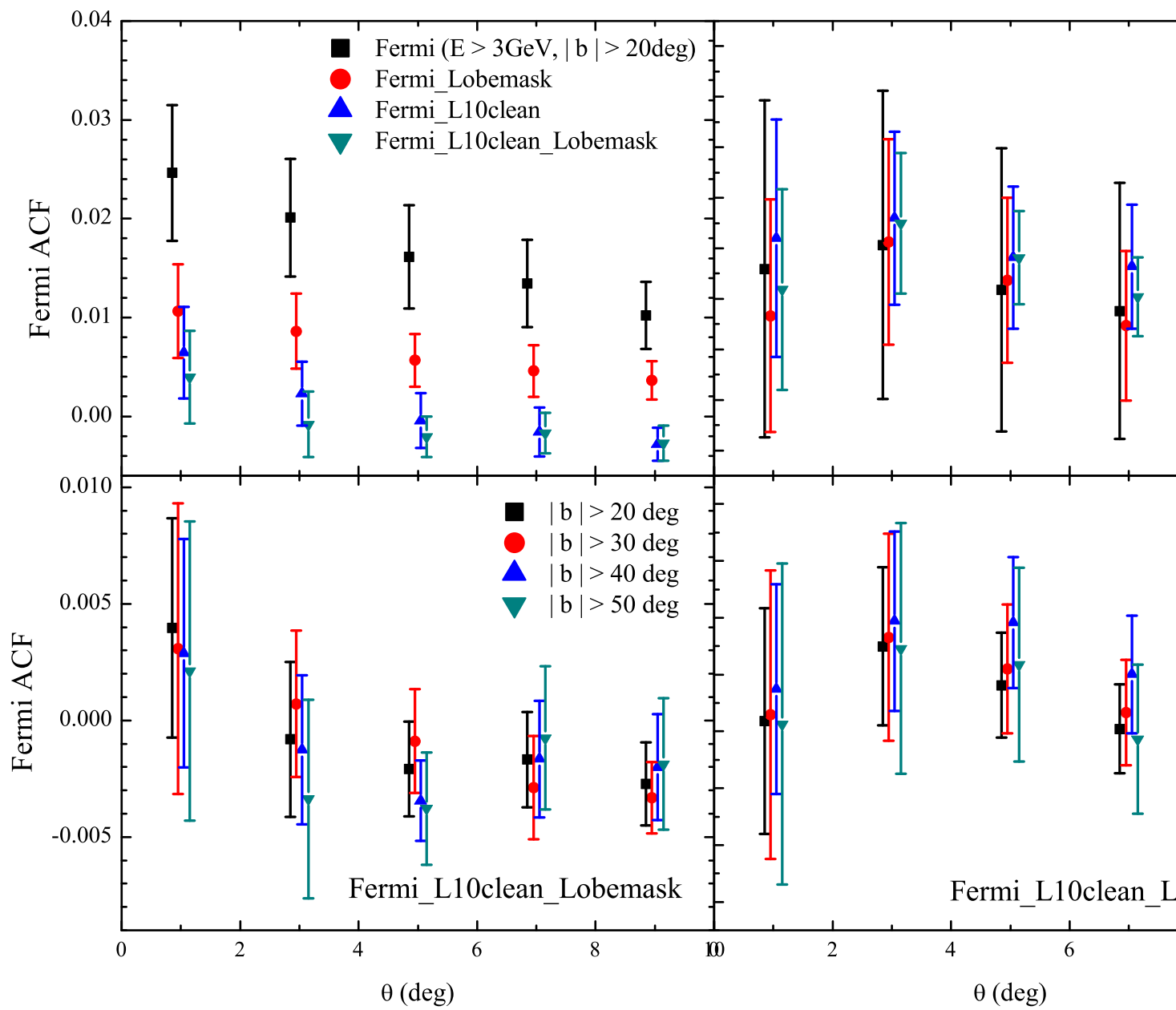
REFERENCES

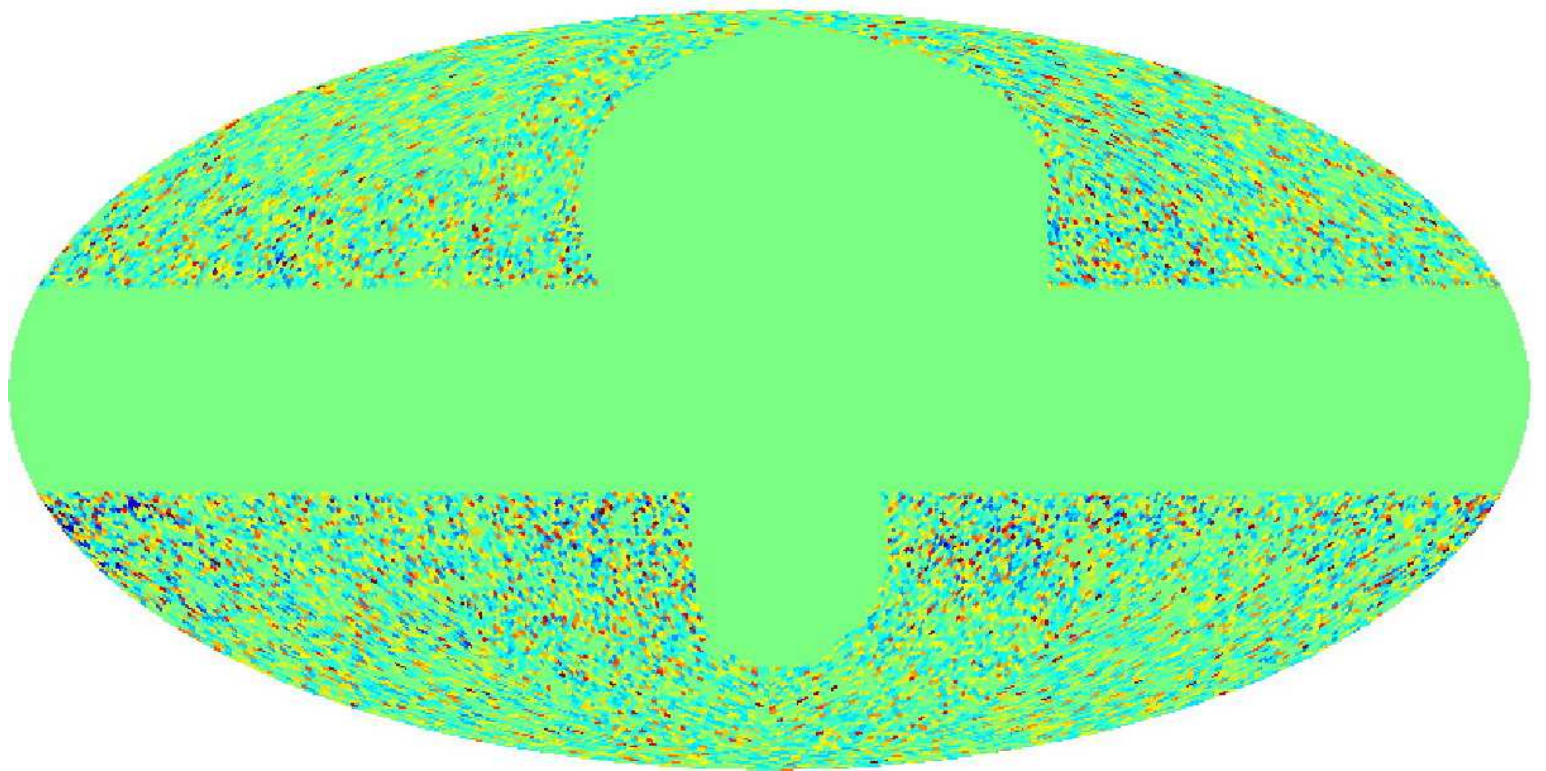
- Abdalla F. B., Banerji M., Lahav O., Rashkov V., 2008, ArXiv e-prints
- Abdo A. A., Ackermann M., et al. 2009, ApJ, 700, 597
- Abdo A. A., Ackermann M., et al. 2010a, JCAP, 4, 14
- Abdo A. A., Ackermann M., et al. 2010b, ApJS, 188, 405
- Abdo A. A., Ackermann M., et al. 2010c, Physical Review Letters, 104, 101101
- Abdo A. A., Ackermann M., et al. 2010d, ApJ, 720, 435
- Ackermann M., Jóhannesson G., Digel S., Moskalenko I. V., Porter T., Reimer O., Strong A., 2008, American Institute of Physics Conference Series, 1085, 763
- Afshordi N., Loh Y., Strauss M. A., 2004, PhRvD, 69, 083524
- Ando S., 2005, Physical Review Letters, 94, 171303
- Ando S., 2009, PhRvD, 80, 023520
- Ando S., Komatsu E., 2006, PhRvD, 73, 023521
- Ando S., Komatsu E., Narumoto T., Totani T., 2007a, MNRAS, 376, 1635
- Ando S., Komatsu E., Narumoto T., Totani T., 2007b, PhRvD, 75, 063519
- Ando S., Pavlidou V., 2009, MNRAS, 400, 2122
- Atwood W. B., Abdo A. A., Ackermann M., Althouse W., Anderson B., Axelsson M., Baldini L., Ballet J., Band D. L., Barbiellini G., et al. 2009, ApJ, 697, 1071
- Baxter E. J., Dodelson S., Koushiappas S. M., Strigari L. E., 2010, ArXiv e-prints
- Blake C., Wall J., 2002, MNRAS, 337, 993
- Bonoli S., Marulli F., Springel V., White S. D. M., Branchini E., Moscardini L., 2009, MNRAS, 396, 423
- Boughn S., Crittenden R., 2004, Nat, 427, 45
- Boughn S. P., Crittenden R. G., Turok N. G., 1998, NewAstron, 3, 275
- Brookes M. H., Best P. N., Peacock J. A., Röttgering H. J. A., Dunlop J. S., 2008, MNRAS, 385, 1297
- Cabr e A., Fosalba P., Gazta naga E., Manera M., 2007, MNRAS, 381, 1347
- Cabr e A., Gazta naga E., Manera M., Fosalba P., Castander F., 2006, MNRAS, 372, L23
- Casandjian J., Grenier I., for the Fermi Large Area Telescope Collaboration 2009, ArXiv e-prints
- Collister A., Lahav O., Blake C., Cannon R., Croom S., Drinkwater M., Edge A., Eisenstein D., Loveday J., Nichol R., Pimblett K., de Propris R., Roseboom I., Ross N., Schneider D. P., Shanks T., Wake D., 2007, MNRAS, 375, 68
- Condon J. J., Cotton W. D., Greisen E. W., Yin Q. F., Perley R. A., Taylor G. B., Broderick J. J., 1998, AJ, 115, 1693
- Cuoco A., Brandbyge J., Hannestad S., Haugb lle T., Miele G., 2008, PhRvD, 77, 123518
- Cuoco A., Hannestad S., Haugb lle T., Miele G., Serpico P. D., Tu H., 2007, JCAP, 4, 13
- Cuoco A., S llerholm A., Conrad J., Hannestad S., 2010, ArXiv e-prints
- de Zotti G., Massardi M., Negrello M., Wall J., 2010, A&ARv, 18, 1
- Dodelson S., Belikov A. V., Hooper D., Serpico P., 2009, PhRvD, 80, 083504
- Fichtel C. E., Kniffen D. A., Hartman R. C., 1973, ApJ, 186, L99+
- Fields B. D., Pavlidou V., Prodanovic T., 2010, ArXiv e-prints
- Fornasa M., Pieri L., Bertone G., Branchini E., 2009, PhRvD, 80, 023518
- Francis C. L., Peacock J. A., 2010, MNRAS, 406, 2
- Gehrels N., 2010, ArXiv e-prints
- Ghisellini G., Maraschi L., Tavecchio F., 2009, MNRAS, 396, L105
- Giannantonio T., Crittenden R. G., Nichol R. C., Scranton R., Richards G. T., Myers A. D., Brunner R. J., Gray A. G., Connolly A. J., Schneider D. P., 2006, PhRvD, 74, 063520
- Giannantonio T., Scranton R., Crittenden R. G., Nichol R. C., Boughn S. P., Myers A. D., Richards G. T., 2008, PhRvD, 77, 123520
- Gold B., Odegard N., Weiland J. L., Hill R. S., Kogut A., Bennett C. L., Hinshaw G., Chen X., Dunkley J., Halpern M., Jarosik N., Komatsu E., Larson D., Limon M., Meyer S. S., Nolta M. R., Page L., Smith K. M., Spergel D. N., Tucker G. S., 2010, ArXiv e-prints
- Gomez Vargas G., on behalf of the Fermi-LAT collaboration Komatsu E., 2010, ArXiv e-prints
- G rski K. M., Hivon E., Banday A. J., Wandelt B. D., Hansen F. K., Reinecke M., Bartelmann M., 2005, ApJ, 622, 759
- Hartman R. C., Bertsch D. L., Bloom S. D., Chen A. W., Deines-Jones P., Esposito J. A., Fichtel C. E., Friedlander D. P., Hunter S. D., McDonald L. M., Sreekumar P., Thompson D. J., Jones B. B., Lin Y. C., Michelson P. F., Nolan P. L., 1999, ApJS, 123, 79
- Hensley B. S., Siegal-Gaskins J. M., Pavlidou V., 2009, ArXiv e-prints
- Hirata C. M., Ho S., Padmanabhan N., Seljak U., Bahcall N. A., 2008, PhRvD, 78, 043520
- Ho S., Hirata C., Padmanabhan N., Seljak U., Bahcall N., 2008, PhRvD, 78, 043519
- Hooper D., Serpico P. D., 2007, JCAP, 6, 13
- Jarrett T., Chester T., Cutri R., Schneider S., Rosenberg J., Huchra J. P., Mader J., 2000, AJ, 120, 298
- Keshet U., Waxman E., Loeb A., 2004, JCAP, 4, 6
- Komatsu E., Smith K. M., Dunkley J., Bennett C. L., Gold B., Hinshaw G., Jarosik N., Larson D., Nolta M. R., Page L., Spergel D. N., Halpern M., Hill R. S., Kogut A., Limon M., Meyer S. S., Odegard N., Tucker G. S., Weiland J. L., 2010, ArXiv e-prints
- Kraushaar W. L., Clark G. W., Garmire G. P., Borken R., Higbie P., Leong V., Thorsos T., 1972, ApJ, 177, 341
- Laureijs R., 2009, ArXiv e-prints
- Lee S. K., Ando S., Kamionkowski M., 2009, JCAP, 7, 7
- Lewis A., Bridle S., 2002, PhRvD, 66, 103511
- Miniati F., Koushiappas S. M., Di Matteo T., 2007, ApJ, 667, L1
- Moskalenko I. V., Porter T. A., 2009, ApJ, 692, L54
- Moskalenko I. V., Porter T. A., Digel S. W., 2006, ApJ, 652, L65
- Moskalenko I. V., Porter T. A., Digel S. W., 2007, ApJ, 664, L143
- Myers A. D., Brunner R. J., Richards G. T., Nichol R. C., Schneider D. P., Vanden Berk D. E., Scranton R., Gray A. G., Brinkmann J., 2006, ApJ, 638, 622
- Nolta M. R., Wright E. L., Page L., Bennett C. L., Halpern M., Hinshaw G., Jarosik N., Kogut A., Limon M., Meyer S. S., Spergel D. N., Tucker G. S., Wollack E., 2004, ApJ, 608, 10
- Pato M., Pieri L., Bertone G., 2009, PhRvD, 80, 103510
- Pavlidou V., Fields B. D., 2001, ApJ, 558, 63
- Pavlidou V., Fields B. D., 2002, ApJ, 575, L5
- Pieri L., Bertone G., Branchini E., 2008, MNRAS, 384, 1627
- Pieri L., Lavalley J., Bertone G., Branchini E., 2009, ArXiv e-prints

- Raccanelli A., Bonaldi A., Negrello M., Matarrese S., Tormen G., de Zotti G., 2008, *MNRAS*, 386, 2161
- Rassat A., Land K., Lahav O., Abdalla F. B., 2007, *MNRAS*, 377, 1085
- Richards G. T., Myers A. D., Gray A. G., Riegel R. N., Nichol R. C., Brunner R. J., Szalay A. S., Schneider D. P., Anderson S. F., 2009, *ApJS*, 180, 67
- Richards G. T., Nichol R. C., Gray A. G., Brunner R. J., Lupton R. H., Vanden Berk D. E., Chong S. S., Weinstein M. A., Schneider D. P., Anderson S. F., Munn J. A., Harris H. C., Strauss M. A., Fan X., 2004, *ApJS*, 155, 257
- Sachs R. K., Wolfe A. M., 1967, *ApJ*, 147, 73
- Schlegel D. J., Bebek C., Heeterdks H., Ho S., Lampton M., Levi M., Mostek N., Padmanabhan N., Perlmutter S., Roe N., Sholl M., Smoot G., 2009, *ArXiv e-prints*
- Schlegel D. J., Finkbeiner D. P., Davis M., 1998, *ApJ*, 500, 525
- Scranton R., Johnston D., et al. 2002, *ApJ*, 579, 48
- Siegal-Gaskins J. M., 2008, *JCAP*, 10, 40
- Siegal-Gaskins J. M., for the Fermi-LAT Collaboration Komatsu E., 2010, *ArXiv e-prints*
- Slatyer T. R., Finkbeiner D. P., 2010, *MNRAS*, 405, 1777
- Smith R. E., Peacock J. A., Jenkins A., White S. D. M., Frenk C. S., Pearce F. R., Thomas P. A., Efstathiou G., Couchman H. M. P., 2003, *MNRAS*, 341, 1311
- Sreekumar P., Bertsch D. L., et al. 1998, *ApJ*, 494, 523
- Su M., Slatyer T. R., Finkbeiner D. P., 2010, *ArXiv e-prints*
- Taoso M., Ando S., Bertone G., Profumo S., 2009, *PhRvD*, 79, 043521
- Ullio P., Bergström L., Edsjö J., Lacey C., 2002, *PhRvD*, 66, 123502
- Xia J., Viel M., Baccigalupi C., Matarrese S., 2009, *JCAP*, 9, 3
- Xia J.-Q., Bonaldi A., Baccigalupi C., De Zotti G., Matarrese S., Verde L., Viel M., 2010, *JCAP*, 8, 13
- Zavala J., Springel V., Boylan-Kolchin M., 2010, *Mon. Not. Roy. Astron. Soc.*, 405, 593
- Zavala J., Vogelsberger M., Slatyer T. R., Loeb A., Springel V., 2011, *ArXiv e-prints*
- Zhang P., Beacom J. F., 2004, *ApJ*, 614, 37

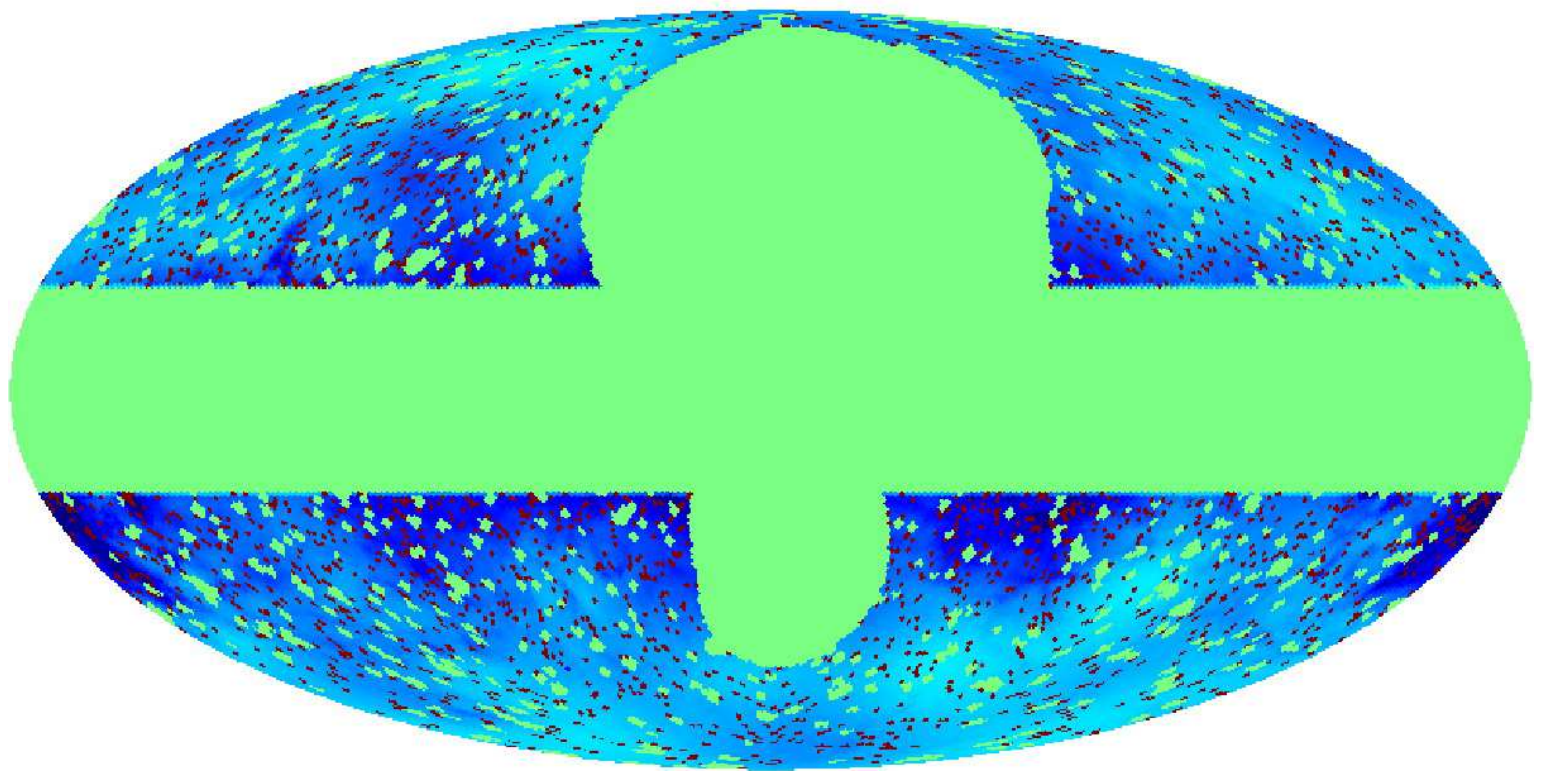


-4.0  4.0

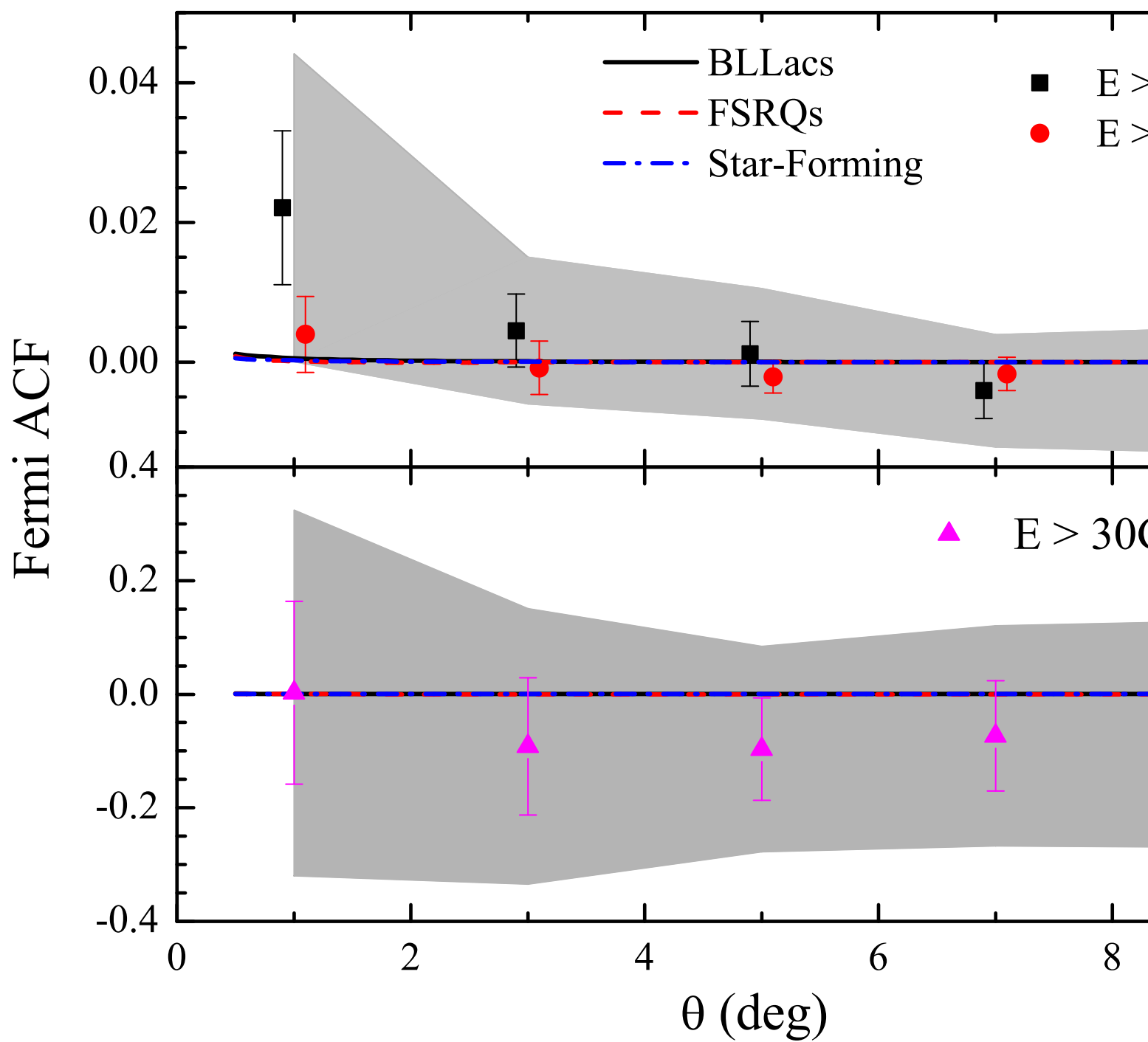




-4.0  4.0



-4.0 4.0



point sources mask and GP ± 20 deg

